Monthly Notices of the ROYAL ASTRONOMICAL SOCIETY

MNRAS **549,** 1–18 (2026)
Advance Access publication 2026 May 15

https://doi.org/10.1093/mnras/stag930

Modelling magnetohydrodynamic waves in a helmet streamer: first comparison with Metis observations

A. Kumar [1]★ S. Daley-Yates [1] T. A. Howson [1,2] P. Pagano,[1,3,4] I. De Moortel[1] and V. Andretta [5]

[1]*School of Mathematics and Statistics, University of St Andrews, St Andrews, Fife KY16 9SS, UK*
[2]*Faculty of Design, Informatics and Business, Abertay University, Bell Street, Dundee DD1 1HG, UK*
[3]*Dipartimento di Fisica & Chimica, Università degli Studi di Palermo, Via Archirafi 36, I-90123 Palermo, Italy*
[4]*INAF – Osservatorio Astronomico di Palermo, Piazza del Parlamento 1, I-90134 Palermo, Italy*
[5]*INAF – Osservatorio Astronomico di Capodimonte, Salita Moiariello 16, I-80131 Naples, Italy*

Accepted 2026 May 12. Received 2026 May 4; in original form 2025 December 13

ABSTRACT

Magnetohydrodynamic waves are often regarded as efficient pathways for magnetic energy transfer from the solar interior. Consequently, they are key not only to understanding the physical processes behind coronal heating and solar wind acceleration but also serve as useful diagnostic tools. While Alfvén wave modes can be difficult to detect directly by remote sensing – due to their incompressive nature – magnetoacoustic wave modes perturb the density and temperature as they propagate. Recently, observations from the Metis coronagraph on board *Solar Orbiter* have shown the ubiquitous presence of propagating density fluctuations in a helmet streamer with a 5-min period. Using 2.5D MHD simulations, we find that such density fluctuations can be generated either from non-linear Alfvén waves or directly from magnetoacoustic waves. Furthermore, density fluctuations generated from Alfvén waves have a doubled frequency with respect to the driven Alfvén wave frequency because of non-linear ponderomotive forces. In general, we find that in a low-β region, the dominant contribution to the density fluctuations is from slow waves propagating along the magnetic field. In a high-β region, the density fluctuations are likely associated with a mixture of both slow and fast waves.

Key words: MHD – waves – Sun: corona – Sun: oscillations – solar wind.

1 INTRODUCTION

A magnetized medium such as the solar atmosphere can host a variety of magnetohydrodynamic (MHD) waves, which are usually a combination of the three fundamental waves modes in MHD – Alfvén, and fast and slow magnetoacoustic. A key difference between these wave modes is how the medium is perturbed and their propagation depends on the background properties of the medium. Several space-based observations have revealed that MHD waves are ubiquitous in various layers of the solar atmosphere and in different magnetic structures such as streamers, filaments, and loops (e.g. J. Cirtain et al. 2007; B. De Pontieu et al. 2007; D. Banerjee, D. Pérez-Suárez & J. Doyle 2009; D. Jess et al. 2015; T. S. Horbury et al. 2020; D. Banerjee et al. 2021; D. B. Jess et al. 2023, and references therein).

MHD waves in the solar atmosphere can originate from the (random) buffeting of the magnetic field lines embedded in the solar surface, also aided by supergranular flows. Pressure waves (known as *p*-mode waves) can also excite waves that propagate into the atmosphere (e.g. H. Spruit & T. Bogdan 1992, for magnetoacoustic waves from sunspots). On the global scale, wave propagation is modified by the magnetic field configuration and gravitational stratification. For example, gravitational stratification imposes an acoustic cutoff such that frequencies lower than 3 mHz (corresponding to the global solar *p*-mode) are filtered out and only higher frequencies can propagate through the upper layers of the atmosphere (see e.g. T. Felipe & C. Sangeetha 2020, and references therein). However, this cutoff may vary by altering the magnetic field strength and also its inclination with respect to the direction of wave propagation (S. M. Jefferies et al. 2006; M. Stangalini et al. 2011).

Despite this acoustic cutoff at the base of the solar atmosphere, 5-min oscillations have been observed in the corona and the solar wind, for example, from the Metis coronagraph on board *Solar Orbiter* (V. Andretta et al. 2025), and also *in situ* in the solar wind from the *Parker Solar Probe* (Z. Huang et al. 2026). In V. Andretta et al. (2025), the authors have shown the persistent propagation of density fluctuations – manifested as intensity fluctuations in white light – up to 2.3 $R_\odot$ with frequencies ranging between 3 and 5 mHz and amplitudes on the order of ~ 0.1 per cent of the coronal background density. This study not only reveals the presence of wave-like density fluctuations, but also reveals a similarity in their propagation in different magnetic field configurations of a helmet streamer and a pseudo-streamer – as propagation speeds range between 150 and 450 km s^{-1} along different probe slits. Notably, these apparent propagation speeds are within the range of values of the characteristic speeds – solar wind, sound and Alfvén speeds – in the middle corona.

★ E-mail: ak394@st-andrews.ac.uk

© The Author(s) 2026.
Published by Oxford University Press on behalf of Royal Astronomical Society. This is an Open Access article distributed under the terms of the Creative Commons Attribution License (https://creativecommons.org/licenses/by/4.0/), which permits unrestricted reuse, distribution, and reproduction in any medium, provided the original work is properly cited.

Downloaded from https://academic.oup.com/mnras/article/549/3/stag930/8679174 by Universita di Palermo - Dipartimento di Scienze Botaniche user on 06 July 2026

The unprecedented observation of the presence of magnetoacoustic waves at such heights opens new avenues for scientific research, including, but not limited to, their generation mechanisms, and their role in coronal heating and/or solar wind acceleration. For example, density fluctuations may be generated by directly perturbing the plasma, producing fast and slow magnetoacoustic wave modes. Alternatively, such density fluctuations may be generated (indirectly) from Alfvén waves via mechanisms such as non-linear ponderomotive effects (J. V. Hollweg, S. Jackson & D. Galloway 1982; E. Verwichte, V. Nakariakov & A. Longbottom 1999), the non-linear generation of magnetosonic waves by Alfvén wave phase mixing (J. Heyvaerts & E. R. Priest 1983; V. Nakariakov, B. Roberts & K. Murawski 1997; G. J. Botha et al. 2000; J. Thurgood & J. McLaughlin 2013), or a combination of both, depending on the local plasma characteristics. Although in analytical studies or idealized setups, these mechanisms can be treated separately, in more realistic, complex setups such as the one we are considering in this study, both mechanisms will likely be at play and it may not always be possible to determine which of the two mechanisms is responsible for the generation of density fluctuations. These fluctations can be sites for Alfvén wave reflection, generating counter-propagating waves which can potentially contribute to the formation of small length scales, the generation of MHD turbulence and wave energy dissipation (A. Van Ballegooijen et al. 2011; D. J. Pascoe et al. 2022; A. Kumar et al. 2025).

Although small amplitude torsional Alfvén waves have recently been detected in the solar corona using observations from Cryo-NIRSP on board the Daniel K. Inouye Solar Telescope (DKIST; R. Morton et al. 2026), (torsional) Alfvén (rather than Alfvénic) waves remain difficult to detect directly with remote-sensing observations as perturbations are likely to cancel out along the line of sight, unless suitably high-resolution observations are available. On the other hand, Alfvénic waves have been observed in the lower solar atmosphere using the Coronal Multi-Channel Polarimeter as well as DKIST, with enhanced powers at periods between 3 and 5 min (R. Morton, S. Tomczyk & R. Pinto 2016; R. J. Morton & R. Soler 2025).

In the present work, we have studied the generation of density fluctuations in a helmet streamer-like magnetic field along with a background solar wind flow using 2.5D numerical MHD simulations. We excite wave-like compressive perturbations using both mechanisms discussed above to investigate whether either driver can result in features similar to those observed by Metis and also which observables may be used to distinguish the drivers. The paper is structured as follows. In Section 2, we describe the numerical model, detailing physical considerations and assumptions, initial and boundary conditions and wave drivers. The results due to the different wave drivers are provided in Sections 3.1 and 3.2 and compared in Section 3.3. Finally, discussion and conclusions are provided in Section 4.

2 NUMERICAL SETUP

Our study consists of numerical simulations of MHD waves in a steady background of a helmet streamer. The streamer is set up assuming fully ionized plasma that is spherically expanding in the presence of gravity; the energetics of the plasma are modified by the inclusion of thermal conduction, optically thin radiative cooling and a uniform resistivity ($\eta = 10^{14}\,\mathrm{cm^2\,s^{-1}}$). In addition, an empirical background heating function ($Q_{\rm bg}$) is used to support coronal temperatures and a super-Alfvénic wind. Under such assumptions, the following equations are advanced in PLUTO (A. Mignone et al. 2007):

$$\frac{\partial \rho}{\partial t} + \nabla \cdot (\rho \mathbf{v}) = 0, \tag{1}$$

$$\rho \frac{d\mathbf{v}}{dt} = -\nabla p + \mathbf{j} \times \mathbf{B} + \rho \mathbf{g} + \rho \mathbf{S}_{\rm w}(r, \theta, t), \tag{2}$$

$$\frac{\partial \mathbf{B}}{\partial t} = \nabla \times (\mathbf{v} \times \mathbf{B}) + \eta \nabla^2 \mathbf{B}, \tag{3}$$

$$\frac{\rho^\gamma}{\gamma - 1} \frac{d}{dt}\left(\frac{p}{\rho^\gamma}\right) = -\nabla \cdot \mathbf{q} - n^2 \Lambda(T) + \eta j^2 + Q_{\rm bg}, \tag{4}$$

$$p = \frac{\rho k_B T}{\mu m_p}. \tag{5}$$

Here, ρ, p, $\mathbf{v}$, and $\mathbf{B}$ denote the density, gas pressure, velocity, and magnetic field, respectively. Furthermore, $\mathbf{j}$ denotes the current density (related to the magnetic field as $\mu_0 \mathbf{j} = \nabla \times \mathbf{B}$, with μ_0 being the magnetic permeability of free space). We include a source term, $\mathbf{S}_{\rm w}$, to drive Alfvén and magnetoacoustic waves, described in detail in Section 2.3. The ideal gas law (5) provides closure to the system of equations, where $k_{\rm B}$ is the Boltzmann constant, T is the temperature, m_p is the proton mass and μ denotes the mean molecular weight, chosen to be $0.63\,m_p$.

The heating function used in (4) is defined as in V. Réville, A. Tenerani & M. Velli (2018):

$$Q_{\rm bg}(r) = \frac{f_0}{H_0}\left(\frac{R_\odot}{r}\right)^2 \exp\left(-\frac{r - R_\odot}{H_0}\right), \tag{6}$$

where the scale height, H_0, and the photospheric energy flux, f_0, are $1\,R_\odot$ and $1.5 \times 10^5\,\mathrm{erg\,cm^{-2}\,s^{-1}}$, respectively, and r denotes the radial coordinate. Such a heating profile results in strong chromospheric heating, eventually driving large upflows and forming the solar wind; the exponential tail is responsible for sustaining the wind at large distances.

We have modelled thermal conduction using the usual Spitzer–Härm approach where

$$\nabla \cdot \mathbf{q} = \kappa_\parallel \hat{\mathbf{B}}(\hat{\mathbf{B}} \cdot \nabla T) + \kappa_\perp \left[\nabla T - \hat{\mathbf{B}}(\hat{\mathbf{B}} \cdot \nabla T)\right]. \tag{7}$$

As the heat conduction in a magnetized plasma is highly anisotropic, we have used $\kappa_\parallel = 9 \times 10^{-7} T^{5/2}\,\mathrm{erg\,cm^{-1}\,s^{-1}\,K^{-1}}$ and $\kappa_\perp = 0$ (E. Priest 2014). The radiative cooling function, $\Lambda(T)$, is derived from J. Klimchuk, S. Patsourakos & P. Cargill (2008).

The physical domain of our simulations starts from the chromosphere at $1\,R_\odot$ and extends up to $20\,R_\odot$, encompassing a small chromospheric layer of 5 Mm and the transition region. Following R. Lionello, J. A. Linker & Z. Mikić (2008) and Z. Mikić et al. (2013), the conduction tensor and cooling function are modified in the transition region as follows:

$$\kappa_\parallel = \begin{cases} \kappa_0 T^{5/2}, & T \geq T_M, \\ \kappa_0 T_M^{5/2}, & T < T_M \end{cases}, \tag{8}$$

$$\Lambda(T) = \begin{cases} \Lambda(T), & T \geq T_M, \\ \Lambda(T)\left(\frac{T}{T_M}\right)^{5/2}, & T < T_M \end{cases}, \tag{9}$$

with $T_M = 2 \times 10^5\,\mathrm{K}$. This ensures a broader transition region, allowing us to resolve the energy flux through this region.

2.1 Initial and boundary conditions

The isothermal hydrostatic chromospheric layer is initialized with a temperature of 10^4 K with a surface number density of $10^{12}\,\mathrm{cm^{-3}}$, which drops to approximately $10^9\,\mathrm{cm^{-3}}$ at 5 Mm above the surface. Above the chromosphere, density, pressure and velocity are derived from Parker's steady-state hydrodynamic solar

Downloaded from https://academic.oup.com/mnras/article/549/3/stag930/8679174 by Universita di Palermo - Dipartimento di Scienze Botaniche user on 06 July 2026

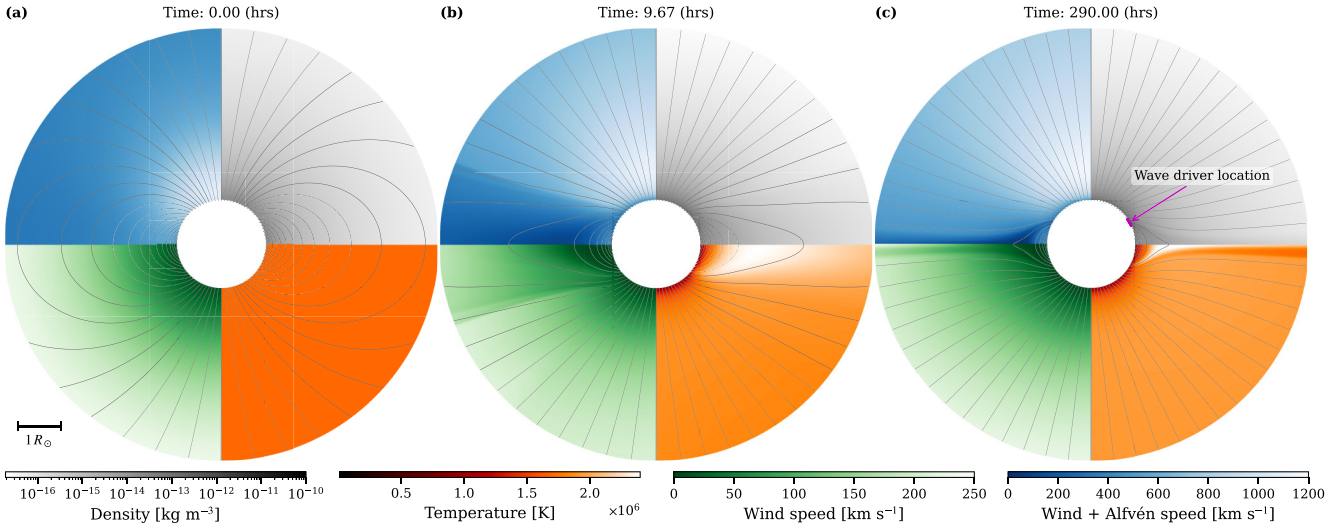

Figure 1. Relaxation of the background plasma in response to an initial dipolar magnetic field. The different colour maps denote, in the clockwise sense, the density, the temperature, the wind speed and finally the Alfvén speed with respect to the background wind speed; magnetic field lines are overplotted in black. The thin magenta patch in (c) indicates the region of wave driving. Note that the simulation domain only spans from 0° to 180° and the other two colour maps are shown for conciseness. An animation showing the formation of a helmet streamer is provided in the online version of this article.

wind (E. N. Parker 1958), assuming a coronal temperature of 1.7×10^6 K for the wind. The Parker wind base density is taken as the number density at the top of the chromosphere. We assume a dipole for the magnetic field, with an equatorial surface magnetic field intensity $B_0 = 1$ Gauss.

$$\mathbf{B}_0(r,\theta) = \frac{2b_0\cos\theta}{r^3}\,\hat{\mathbf{r}} + \frac{b_0\sin\theta}{r^3}\,\hat{\theta}. \tag{10}$$

At the lower radial boundary we apply similar conditions to S. Parenti et al. (2022), where density, magnetic field and velocity are static in the ghost cells and a layer of cells (equal to the number of ghost cells) above the boundary is modified so that the poloidal velocity (v_r, v_θ) is parallel to the poloidal magnetic field (B_r, B_θ). See fig. 1 of S. Parenti et al. (2022) for details. A key difference from S. Parenti et al. (2022) is that our numerical domain contains a chromospheric layer acting as a hydrostatic, isothermal mass reservoir, which requires a static pressure in the ghost cells. Lastly, $dB_\phi/dr =$ constant sets the condition on B_ϕ. At the outer radial boundary, ρr^2, pr^2, ρv_r, v_θ, rv_ϕ, $B_r r^2$, B_θ and rB_ϕ are all held constant. The boundary conditions in the θ-direction are set to PLUTO's predefined 'axisymmetric' boundaries.

The above-described setup is advanced on a two-dimensional grid in spherical co-ordinates on the $r-\theta$ plane. The radial grid starts from 1 $R_\odot$ and extends until 20 $R_\odot$, consisting of 2816 grid cells distributed as follows. The first 128 cells are spread uniformly in the first 10 Mm, forming the chromosphere and the transition region. This is followed by a stretched grid – whose stretching factor is calculated using the adjacent uniform grid to ensure a smooth transition – until 2.4 $R_\odot$ utilizing 1536 cells. The remaining 1152 cells are logarithmically stretched until 20 $R_\odot$. In the θ-direction, we have used 1920 uniformly spaced cells from 0° to 180°. Such high resolution is required to numerically resolve wavelengths ranging between 0.1 $R_\odot$ and 0.4 $R_\odot$ – corresponding to the 5-min global p-mode of the Sun – with roughly 100 cells near the equator and 400 cells near the poles where the propagation speed is higher.

For time evolution, we have used the second-order Runge–Kutta solver along with linear spatial reconstruction via the van Leer slope limiter, and the Harten, Lax, van Leer (HLL) Riemann solver. The $\nabla \cdot \mathbf{B} = 0$ condition is imposed using Powell's eight-wave formalism and, finally, resistivity and thermal conduction are handled using the second-order RK-Legendre scheme.

2.2 Relaxation and evolution to a helmet streamer

The combination of the Parker wind initial conditions and the initial dipole magnetic field configuration is not an equilibrium setup. Additionally, thermal conduction and radiative cooling tend to smooth out any discontinuity in temperature and density. As such, we perform a numerical relaxation to attain conditions suitable for subsequent studies of wave dynamics. During this relaxation, the imposed heating powers a fast, hot solar wind. In regions close to the equator, this plasma outflow stretches the closed magnetic field lines, forming a streamer structure with a hot and dense core. In contrast, polar regions offer lower amounts of magnetic tension (across the magnetic field lines), resulting in higher wind speeds and lower plasma densities.

After $\sim$ 12 d of simulated time, our simulation attains a steady state; the evolution during this phase is shown in the three panels of Fig. 1. Because of the complex distribution of the wind speed and plasma density across latitudes, the wind becomes super-Alfvénic at $\sim 11\,R_\odot$ near the poles and at $\sim 2\,R_\odot$ near the equator.

2.3 Wave drivers

The simulations presented in this article aim to study the wave-like density fluctuations associated with propagating MHD waves in a helmet streamer configuration. Such fluctuations have been inferred from Metis white light coronagraphic observations (V. Andretta et al. 2025). Therefore, we study the effects of different wave driving mechanisms which can induce such plasma compressions.

Downloaded from https://academic.oup.com/mnras/article/549/3/stag930/8679174 by Universita di Palermo - Dipartimento di Scienze Botaniche user on 06 July 2026

To drive waves in our model, we include a source term ($\mathbf{S}_\mathrm{w}$) in the momentum equation (2), as in H. Van Damme et al. (2020) and H. Callingham, I. De Moortel & P. Pagano (2024). Using such a driver allows us to drive both Alfvén ($\mathbf{S}_\mathrm{w} = S_\mathrm{w}\hat{\phi}$) and magneto-acoustic wave modes ($\mathbf{S}_\mathrm{w} = S_\mathrm{w}\hat{\theta}$) by merely altering the direction of perturbation. We define this source term as the product of two Gaussian functions – centred at (r_0, θ_0) – and a sinusoidal term:

$$S_\mathrm{w}(r,\theta,t) = A_0 \exp\left[-\left(\frac{r-r_0}{\sigma_r}\right)^2\right] \exp\left[-\left(\frac{\theta-\theta_0}{\sigma_\theta}\right)^2\right] \sin\omega t, \tag{11}$$

which is spread over a region defined by σ_r and σ_θ. This ensures a localized region from where MHD waves can be excited. A localized transverse driver for which $\mathbf{S}_\mathrm{w} = S_\mathrm{w}\hat{\theta}$ will directly compress the plasma as the applied perturbation is in the plane of the simulation. On the other hand, Alfvén waves will be generated if the driver is applied in the invariant direction, $\mathbf{S}_\mathrm{w} = S_\mathrm{w}\hat{\phi}$. These will be incompressible in the linear limit. However, for non-linear Alfvén waves, ponderomotive forces will excite plane-parallel compressive perturbations and induce density variations too (e.g. E. Verwichte et al. 1999).

Note that A_0 has dimensions of acceleration and the resultant wave amplitude is determined by the system's response to this term. For the Alfvén wave case ($\mathbf{S}_\mathrm{w} = S_\mathrm{w}\hat{\phi}$), we select A_0 such that the generated waves are weakly non-linear. As a result, due to the ponderomotive force, these drive density perturbations of approximately $\sim 3{-}4$ per cent (as described in more detail below). When applied in the latitudinal θ-direction, the driver amplitude is again tuned such that the density fluctuations roughly match these values.

For the simulations reported in this work, we have confined the driver to a narrow region just above the chromosphere ($r_0 = 1.025\,R_\odot$, $\sigma_r = 5\times10^{-4}\,R_\odot$) at the interface between open and closed magnetic field lines ($\theta_0 = 60^\circ, \sigma_\theta = 5^\circ$), indicated by a thin magenta patch in Fig. 1(c).

A perturbation to the local velocity as described above usually results in two wave components that propagate in opposite directions from the source. However, due to higher densities towards the chromosphere, inward propagating waves are either damped or reflected, and only outward propagating waves remain. We note that the reflected waves may interact with the driver region, and can result in a period of the propagating waves that is different from the driver (H. Callingham et al. 2024).

After a steady state has been reached for the initial setup, the simulations are restarted with the driver and advanced for the next 12 h, with outputs every 30 s of simulated time. The timestamps shown in our results denote the times corresponding to the wave simulation. Also note that our region of interest lies in the middle corona and therefore, the figures are truncated to $4\,R_\odot$ in most cases, and projected onto Cartesian coordinates.

3 RESULTS

Before comparing and contrasting the density perturbations excited by these wave modes, we first describe the results of each of the simulations separately.

3.1 Driver in the invariant ϕ-direction

Periodic perturbations applied along the invariant ϕ-direction produce Alfvén waves with an initial amplitude of $\sim 40\,\mathrm{km\,s^{-1}}$ near the driver region, i.e. in the low corona. A snapshot of the v_ϕ perturbations at $t = 250$ min is shown in Fig. 2(a). For this simulation, the wave driver has a period of 10 min, amplitude of $8.62\,\mathrm{km\,s^{-2}}$ and is applied at the interface between open and closed magnetic field lines. This equatorially asymmetric choice of driver location allows us to study the wave propagation in different regions of the domain.

In our simulated atmosphere, as the Alfvén waves propagate along the magnetic field lines, they encounter significant changes in the local Alfvén speed due to a combination of changes in the density and magnetic field strength. Their propagation speed is further modified by the background wind. This can result in either wave amplification, damping or reflection depending on the background medium (e.g. D. Yuan et al. 2015; D. J. Pascoe et al. 2022; A. Kumar et al. 2025). For example, in the open field region we see the wave amplitudes increase monotonically. On the other hand, waves propagating along field lines passing through the dense streamer encounter large density gradients resulting in continuous partial reflections (see Fig. 2(b), which shows the counter-propagating Alfvén wave component). The higher density and weaker magnetic field near the streamer cusp also means that the Alfvén speed (and therefore the wavelength) reduces. In this region, there is a decay in Alfvén wave amplitude which results in a loss of Alfvén wave signature south of the equator in the majority of the domain. This is caused by a combination of effects, including enhanced dissipation due to phase mixing and decreasing field-aligned length scales, wave reflection driven by density inhomogeneities, mode conversion of Alfvén waves into slow waves due to the ponderomotive force and field line expansion. As part of the Alfvén amplitude decay is due to non-linear effects, it is possible that Alfvén waves with small amplitudes could travel closer to the streamer cusp.

On closed field lines at lower altitudes, Alfvén waves do not encounter such a significant reduction in the Alfvén speed and are therefore able to cross the equator. As they encounter the chromosphere at the other footpoint, which acts as a rigid boundary, they undergo significant reflections. Eventually, we find a mixture of counter-propagating Alfvén waves along these field lines – this is evident from large non-zero values of $z^- \left(= v_\phi - B_\phi/\sqrt{\mu_0\rho}\right)$ in Fig. 2(b), denoting Alfvén waves propagating in a direction opposite to the guide magnetic field. From Fig. 2(a), we can see that the maximum amplitude for the Alfvén waves is about $80\,\mathrm{km\,s^{-1}}$ and occurs near the apex of the closed field regions, at $\sim 1.3\,R_\odot$. Elsewhere in the domain, the peak wave amplitudes are of the order $\sim 50\,\mathrm{km\,s^{-1}}$, occurring just north of the streamer. These amplitudes are consistent with observations of coronal Alfvénic perturbations reported by (e.g. S. W. McIntosh & B. De Pontieu 2012; M. J. Weberg, R. J. Morton & J. A. McLaughlin 2018; R. Morton, M. Weberg & J. McLaughlin 2019).

3.1.1 *Generation of density fluctuations via Alfvén wave mode conversion*

Although Alfvén waves are incompressible in the linear limit, non-linearity leads to the excitation of compressible (density) perturbations via ponderomotive forces and/or phase mixing. These density perturbations are associated with slow and fast waves. In our simulations, we find density fluctuations of the order of $\sim 3{-}4$ per cent of the background density, which can be clearly seen as running differences between simulation outputs, shown in Fig. 2(c). Since our simulation domain has a wide range of

Downloaded from https://academic.oup.com/mnras/article/549/3/stag930/8679174 by Universita di Palermo - Dipartimento di Scienze Botaniche user on 06 July 2026

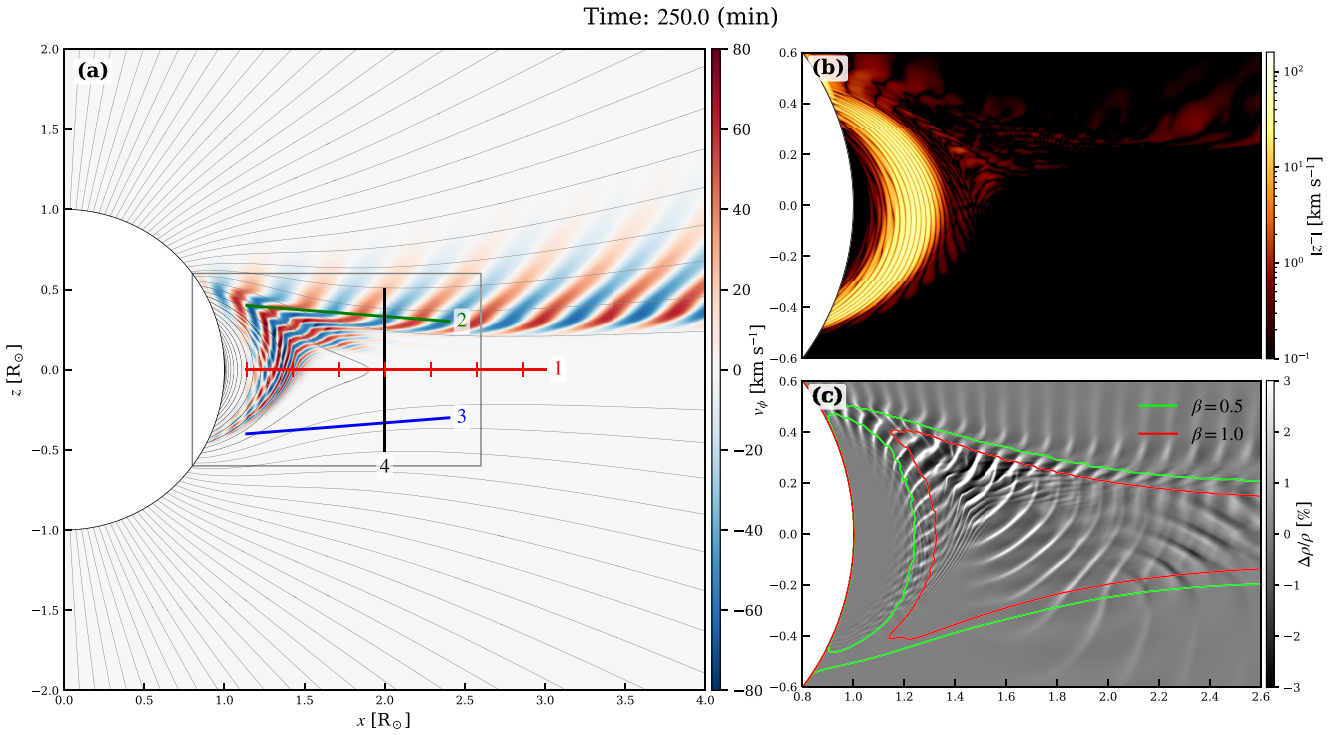

Figure 2. **(a)** Alfvén wave propagation in the domain for a driver placed at the interface between open and closed magnetic field lines. The straight lines numbered 1 through 4 denote the slits used for the analysis discussed in further sections. In slit 1, the markers are drawn at every 200 Mm for ease of comparison with subsequent time–distance plots. The black box denotes the sub-domain plotted in (b) and (c). **(b)** A contour map of the Elsässer variable z^-, denoting regions where Alfvén waves propagate in the opposite direction with respect to the guide magnetic field. **(c)** Density fluctuations induced due to the non-linearity of Alfvén waves; the solid lines denote contours for $\beta = 0.5$ and $\beta = 1$. An animation showing the propagation of Alfvén waves and associated density fluctuations is provided in the online version of this article.

plasma β values – the lowest near the poles and the highest near the streamer cusp – density fluctuations are expected to have different amplitudes in different plasma β regimes. This is illustrated in Appendix A through a separate set of simple simulations for different values of the plasma β which show that in a locally homogenous plasma, the density fluctuations resulting from the ponderomotive force will have higher amplitudes in regions with lower plasma β. For ease of reference, we simply refer to slow and fast waves throughout this paper but it is useful to remember that these waves take on different characters in high and low-beta regimes. When $\beta \ll 1$, the fast wave is mostly magnetic whereas the slow wave has a largely acoustic character. These characteristics reverse in a low-β regime, where the slow wave is predominately magnetic in character and the fast wave becomes acoustic (see e.g. H. Schunker & P. S. Cally 2006).

Once generated, the density fluctuations propagate, displaying either slow or fast characteristics, while also being continuously generated due to the propagating non-linear Alfvén waves. This is illustrated in Fig. 3, where induced plane-parallel velocities are decomposed into components that are parallel and perpendicular to the local magnetic field. In low-β regions, the parallel and perpendicular components correspond largely to the slow and fast waves, respectively. In the high β regime, distinguishing the slow and fast waves is less straightforward (note the similarity in the profiles of the perturbations for the insets in Fig. 3). Although the perpendicular component still corresponds to the fast wave, the parallel velocity component will be a mixture of the slow and fast waves. Comparing the density fluctuations in Fig. 2(c) with the decomposed velocities in Fig. 3, it is clear that the slow waves are the main contribution to the density perturbations just north of the streamer whereas in the streamer core, both the slow and fast waves contribute.

The density fluctuations associated with the fast waves can propagate across the magnetic field. This is particularly apparent within the high-β region (the region inside the red $\beta = 1$ contour in Fig. 2(c)). Within this region, the density perturbations propagate across field lines, filling the equatorial region, including the streamer core (which is inaccessible to the Alfvén waves that drive these density perturbations). Across the $\beta = 1$ layer, there are large gradients in the background density and hence the local wave speed. As a result, we see greater reflection and refraction around this layer. This induces complex wave dynamics including wave interference, similar to those found in observations (V. Andretta et al. 2025). There is a clear pattern of refraction and reflection in both the perpendicular and parallel velocity components inside the streamer region and transmission of the perpendicular velocity component into the area south of the streamer. As this is again a low-β region, these density fluctuations south of the streamer are associated with the fast wave. The presence of fast (magnetic) waves in the low-β region south of the streamer is most likely due to conversion across the $\beta = 1$ layer of fast acoustic to fast magnetic waves although as shown by H. Schunker & P. S. Cally (2006), conversion from slow magnetic (in the high-β region) to fast magnetic (in the low-β region) is also possible under certain conditions (e.g. for certain inclination angles of the magnetic field or thin equipartition layers).

Downloaded from https://academic.oup.com/mnras/article/549/3/stag930/8679174 by Universita di Palermo - Dipartimento di Scienze Botaniche user on 06 July 2026

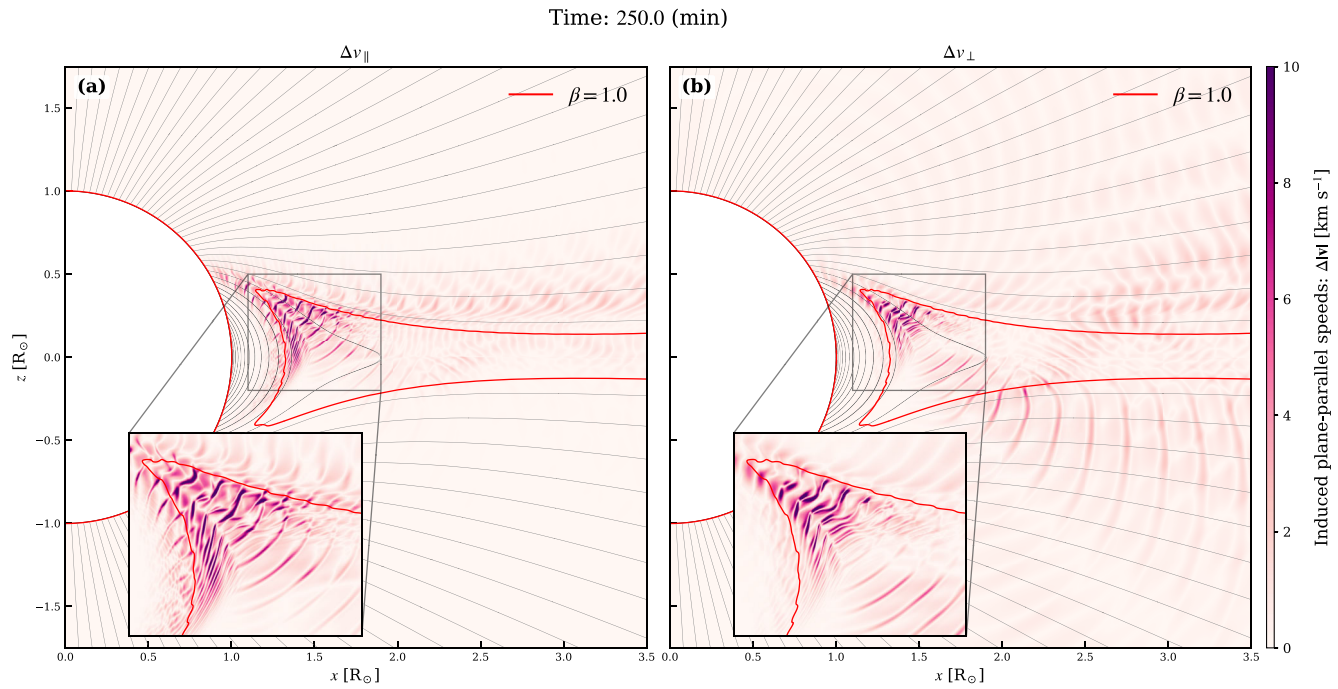

Figure 3. Decomposition of the non-linearly induced plane-parallel velocities into components parallel (**left**) and perpendicular (**right**) to the local magnetic field for the Alfvén wave simulation.

3.1.2 Time–distance analysis

In order to compare how the perturbations we study would potentially be observed in Metis' coronagraphic observations, we analyse our simulations along four different slits in the domain, shown in Fig. 2(a), numbered 1 through 4. As the primary goal of our study is to compare with the Metis observations of V. Andretta et al. (2025), the slits are chosen to (approximately) match their observational analysis. The first and the fourth slits sample cells along and across the equator, respectively, whereas slits 2 and 3 are placed symmetrically about the equator such that they are approximately parallel to the majority of the magnetic field lines sampled along them. We use these slits as probes to create time–distance plots; for example, the plots corresponding to slit 1 are shown in Fig. 4. Before we describe our detailed analysis of waves along different slits, we note that the time–distance plots shown in Fig. 4 do not necessarily show wave propagation along these slits; they rather denote wave arrival at those locations. This is because neither the Alfvén wave nor the associated density fluctuations propagate parallel to the slits. The Alfvén waves strictly propagate along magnetic field lines, and the density fluctuations (associated with the slow and fast wave modes) propagate anisotropically through the magnetized plasma. As a result, there might be a disagreement between the measured apparent propagation speed along a slit and the local wave speeds. However, these apparent propagation speeds are useful to explain and compare with observational results for which the local plasma parameters and magnetic structures remain poorly constrained.

Fig. 4(a) illustrates the arrival of Alfvén waves along an equatorial slit and the corresponding propagating density fluctuations in Fig. 4(b). The density fluctuations are calculated by taking a running difference between successive outputs, normalized by the previous output. While the middle panel shows density fluctuations in simulations, the right panel (Fig. 4(c)) shows the fluctuations in density integrated along a line of sight parallel to the rotationally invariant ϕ-direction. In order to calculate the line-of-sight integrated densities, we assume axial symmetry and rotate the two-dimensional simulation plane about the north–south axis to construct a three-dimensional volume. As the white light emission observed by Metis scales linearly with the density, the line-of-sight integrated density can be compared qualitatively with the Metis observations. Hence, to estimate the synthetic Metis intensity, we calculate:

$$\int_l \rho \, \mathrm{d}l, \tag{12}$$

where the integral is calculated along lines of sight (denoted by l) perpendicular to the simulation plane (the plane of the sky). Due to the line-of-sight integration, projection effects will be present, leading to deviations between the line-of-sight-integrated densities and those obtained directly from the simulations.

Note that while the white-light coronagraphic observations provided by Metis reveal the distribution of density of the plasma surrounding the Sun, it does not provide Doppler velocities and magnetic field fluctuations to directly observe (linear) Alfvén waves. However, intensity fluctuations due to weakly non-linear Alfvén waves may be observed. Therefore, the time–distance maps of the line-of-sight intensity fluctuations presented in our article may be compared with those in fig. 3 of V. Andretta et al. (2025), for example.

In Fig. 4(a), we once again note the confinement of Alfvén waves to lower heights in the closed field region as the Alfvén waves do not penetrate the region above the helmet streamer. On the other hand, density fluctuations associated with the Alfvén waves can fill the domain and are thus observed in regions which

Downloaded from https://academic.oup.com/mnras/article/549/3/stag930/8679174 by Universita di Palermo - Dipartimento di Scienze Botaniche user on 06 July 2026

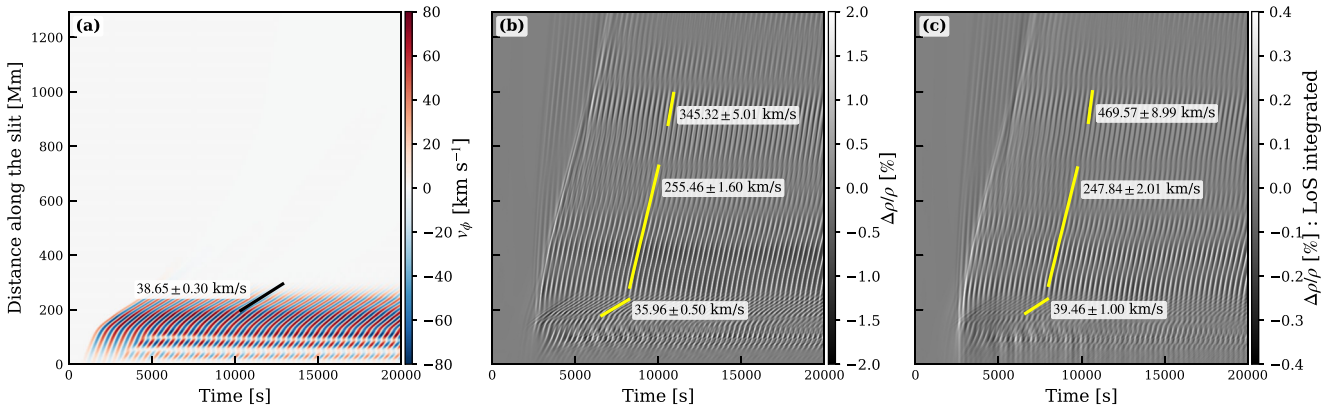

Figure 4. Time–distance maps along slit 1 for **(a)** the Alfvén wave perturbation, **(b)** running difference of the density, and **(c)** running difference of the line-of-sight integrated density for the driver in the ϕ-direction. The black and yellow lines indicate the tracked bright features, used to estimate the apparent propagation speeds, also indicated alongside.

Alfvén waves cannot access (e.g. compare Figs 4(a) and 4(b) above 300 Mm along the slit). The time–distance plots can also be used to estimate apparent propagation speeds by tracking the bright and dark features – indicated by solid lines on the plots. The (apparent) propagation speed is given by the inclination of these bright and dark features in the time–distance plots. Note that the feature being tracked is arbitrarily chosen as they are all mostly parallel to each other. Along the equator, between ∼ 150 and 250 Mm, both the Alfvén wave perturbation (left) and the density fluctuations (middle) are observed to propagate at approximately the same speed of $\sim 40\,\mathrm{km\,s^{-1}}$. This similarity in the propagation speeds – for the waves as well as the density fluctuations – suggests that the density fluctuations appear spontaneously when Alfvén waves arrive at those locations.

The estimated apparent propagation speeds for distances 150−300 Mm along the slit correspond to the speed at which Alfvén perturbations are expected to propagate in the presence of a background solar wind flow ($v_\mathrm{A} + v_\mathrm{sw}$, Fig. 5(a)). This is because of the approximately radial magnetic field configuration at the helmet streamer cusp that Alfvén waves briefly follow the equatorial slit before their amplitudes decay because of the effects mentioned above. At even lower heights along the slit (< 150 Mm), the apparent speeds appear to be higher. However, as the magnetic field lines are perpendicular to the equatorial slit these speeds are not actually propagation speeds but times at which the Alfvén waves cross the slit.

At higher altitudes along the equator ($> 300-400$ Mm), density fluctuations are not generated *in situ* as these regions remain inaccessible to Alfvén waves. Instead, they are associated with the slow and fast waves which travel from either the north of the streamer or are reflected within the streamer core. As these fluctuations are advected by the background wind and as they transition to the high β regime (~ 200 Mm, see Fig. 5(b)), their propagation becomes isotropic and the slow and fast modes become difficult to distinguish in the density running difference plots. We find from the time–distance plots that the apparent propagation speeds for altitudes > 300 Mm range between 250 and 380 $\mathrm{km\,s^{-1}}$, which is in agreement with the local sound speed (Fig. 5(a)). However, the time–distance plots capture the arrival of density fluctuations at those locations due to a combination of slow and fast magnetoacoustic waves. As demonstrated

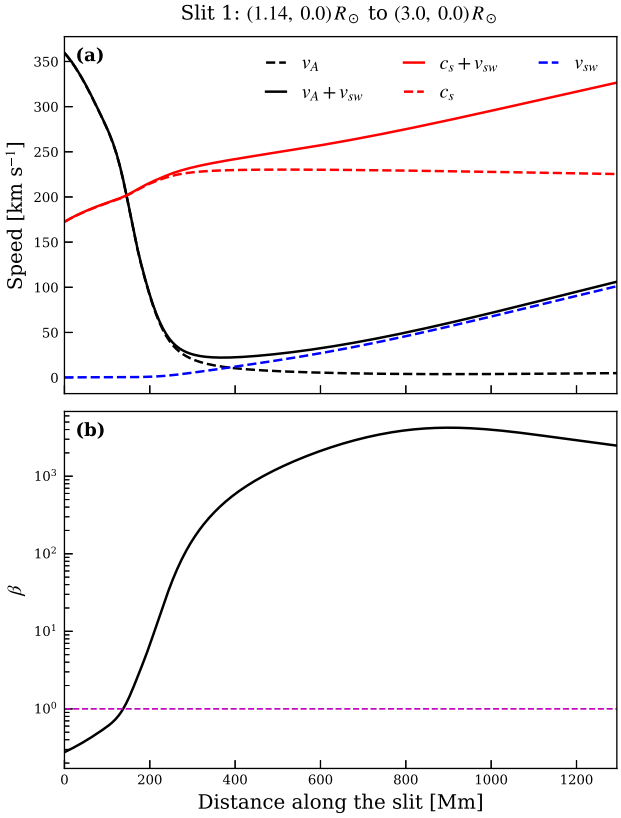

Figure 5. **(a)** Characteristic speeds and **(b)** plasma β along the equatorial slit labelled as slit 1 in Fig. 2(a).

in Appendix C, for this slit (slit 1), there are approximately equal contributions from both wave modes.

Lastly, we note that the normalized running difference of the densities decreases when a line-of-sight integration is carried out (compare Fig. 4(b) and Fig. 4(c)). Since this calculation involves projecting the plasma from the plane of sky to the line of sight, there are also contributions from different heights to the estimated intensity. These contributions are higher for lines of sight

Downloaded from https://academic.oup.com/mnras/article/549/3/stag930/8679174 by Universita di Palermo - Dipartimento di Scienze Botaniche user on 06 July 2026

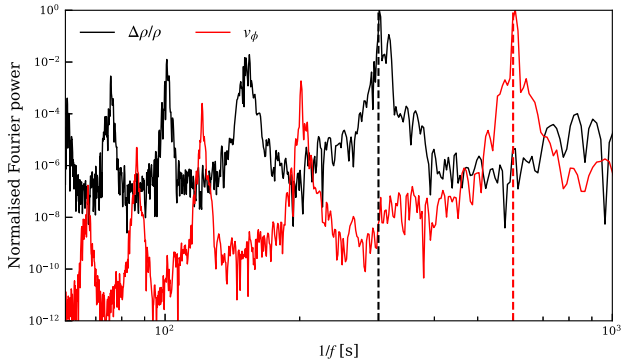

Figure 6. Fourier spectrum of the time series at 150 Mm along slit 1 for the perturbed velocity (v_ϕ; plotted in red) and the corresponding density fluctuations ($\Delta\rho/\rho$; plotted in black). The vertical dashed lines are drawn at the maximum values of these spectra; other peaks corresponding to higher harmonics indicate the presence of (less prominent) complex wave behaviour.

closer to the centre than at the limb since the spherical nature of our numerical domain implies a longer line of sight closer to the centre than at larger heights above the solar surface. Although this is an artificial consequence of the spherical setup, in reality the plasma near the plane of the sky has a higher density and hence, will contribute more to the line-of-sight integrated observables, making this artefact negligible. Despite such effects, the apparent propagation speeds are in agreement with those derived from the actual running differences in density – particularly at higher altitudes where projection effects are minimal.

The ponderomotive origin of the observed density fluctuations is verified by extracting the dominant period in a time series at a given height. Because the ponderomotive force is proportional to the gradient of the excess magnetic pressure ($\mathbf{F}_p \sim -\nabla B_\perp^2$), we expect the density fluctuations to have half the Alfvén wave period. We perform this analysis by taking a time series at a height of 150 Mm along the equatorial slit shown in Fig. 2(a) and taking a Fourier transform, shown in Fig. 6. Maximum power in the spectrum occurs at 10 min for the Alfvén wave component (v_ϕ) which is the same as the period with which waves are driven. For the density fluctuations ($\Delta\rho/\rho$), maximum power occurs at 5 min, which confirms their ponderomotive origin.

In addition to these dominant periods, we find smaller peaks corresponding to higher frequencies as well, which are likely related to small-scale reflections and wave trapping. For Alfvén wave perturbations (v_ϕ), subsequent peaks correspond to the odd harmonics – 200 s, 120 s, 85 s and 67 s. In contrast, for density fluctuations ($\Delta\rho/\rho$), subsequent maxima correspond to the higher harmonics of the dominant (density fluctuation) peak – 150 s, 100 s and 75 s. We note that this might be associated with complex wave behaviour involving continuous reflections and wave interference. As each frequency peak in v_ϕ also has a corresponding doubled frequency in $\Delta\rho/\rho$, it suggests that the non-linear ponderomotive effects are present even for higher Alfvén wave harmonics that generate density fluctuations at half the corresponding period.

3.2 Driver in the latitudinal θ-direction

In the previous section, we examined how density fluctuations are induced by propagating non-linear Alfvén wave modes, excited by applying a driver in the invariant ϕ-direction. We now consider a driver in the latitudinal θ-direction, that excites magnetoacoustic waves which can naturally compress the plasma. The degree of this compression depends on the local plasma β. We note that in this case, the driven waves directly compress the plasma, as opposed to the indirect effect described earlier. In order to produce 5-min wave-like density fluctuations as in Section 3.1, the driving period is set to 5 min; note that this period is half of the Alfvén wave driver period where the density fluctuations are due to non-linear effects. We further note that the amount of wave energy injected into the system due to this momentum driver also depends on the driver frequency – shorter periods inject lower energies over a cycle. Since the driver is naturally compressive, we halve the driver amplitude to 4.31 km s^{-2}. Lastly, the driver location remains unchanged from the previous case. The velocity and density perturbations excited by this magnetoacoustic driver are shown in Fig. 7.

In Fig. 7(a), we show a snapshot of the induced plasma velocities – of up to 10 km s^{-1} – and the resulting density fluctuations in Fig. 7(b), as differences from a previous output 30 s before. Note that the induced perturbations are predominantly in the θ-direction – the same as the direction of the applied perturbation – shown by the black arrows in the inset figure. The equatorial asymmetry is because the driver is located in the Northern Hemisphere. As in Fig. 2(c) (Alfvén wave driver), we see the propagation of magnetoacoustic waves with amplitudes ranging between 4 per cent and 6 per cent, in a background with varying plasma β.

In Fig. 8, we show the decomposition into parallel and perpendicular velocity components. The slow wave components (corresponding to the parallel velocities in low-β parts of the domain) have a similar distribution as in the case of the Alfvén driver (Fig. 3). Despite having a larger distribution in the fast wave component (Fig. 8(b)), the density fluctuations in the northern part of the simulation domain are weaker as the fast mode is less dominant in the low β regime (note that the wave driver, being parallel to the θ-direction, predominantly drives fast waves, since the field is approximately radial). This is also illustrated for a short Alfvén wave pulse in Appendix B. The waves also propagate southwards towards the high-β region near the equator. As seen in the previous section, the density fluctuations generated by Alfvén waves exhibit a similar behaviour, as they undergo mode conversion to slow and fast magnetoacoustic waves. The key difference lies in how these fluctuations are generated – in the former case, plasma compressions occur wherever Alfvén waves exhibit non-linear behaviour; as a result, each point along their propagation acts as a source for density fluctuations. In this scenario of a magnetoacoustic driver, there are no additional sources apart from the driven region. Once generated, these density fluctuations propagate at the fast speed perpendicular to the magnetic field and at the slow speed along the field, on top of the background wind.

As the propagation of these magnetoacoustic pulses slows down close to the equator, the wavefronts arrive almost perpendicularly (see the bright features in Fig. 7(b) in the high β region). This results in a higher apparent propagation speed along an equatorial slit (Fig. 9) when compared to the driver considered in the previous section. In contrast, for an Alfvén wave driver, density fluctuations are also generated *in situ*, within the dense streamer core, from where wavefronts propagate almost parallel to the equator, imparting an overall lower apparent speed.

Downloaded from https://academic.oup.com/mnras/article/549/3/stag930/8679174 by Universita di Palermo - Dipartimento di Scienze Botaniche user on 06 July 2026

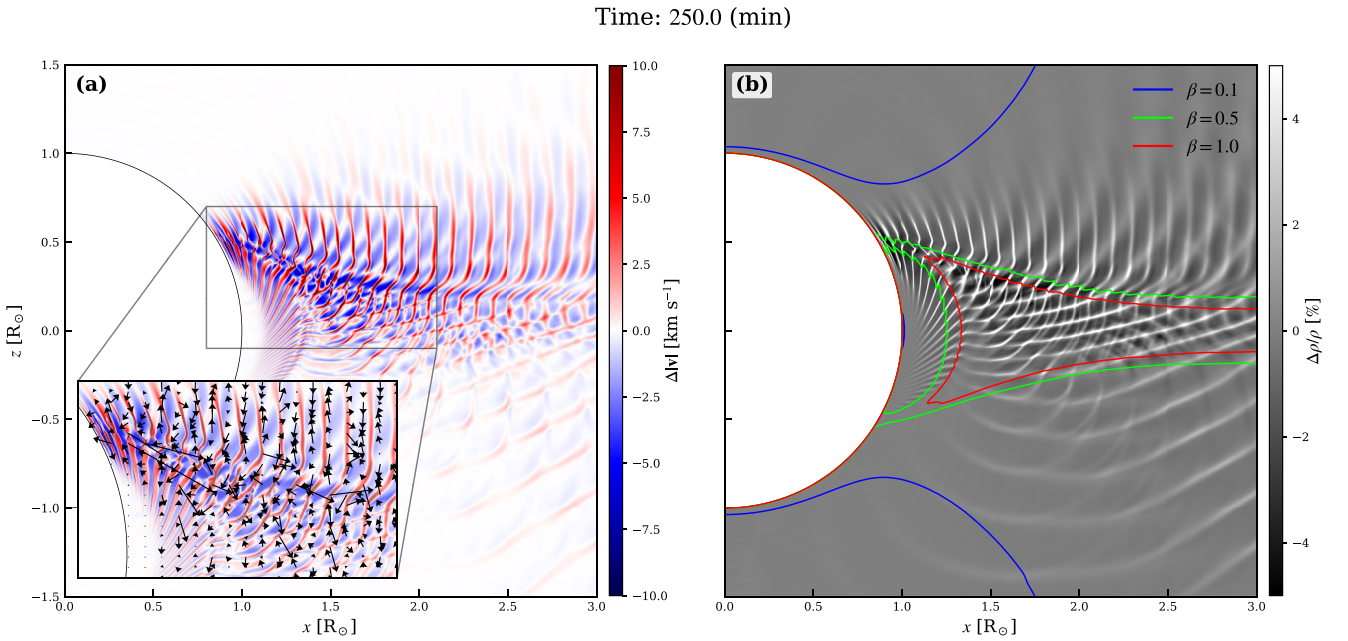

Figure 7. **(a)** Compressive plasma perturbations induced from a magnetoacoustic wave driver, aligned with the θ-direction. The black arrows denote direction of these perturbations while the colours indicate excess plane-parallel speeds as a difference from a previous output. **(b)** Corresponding density fluctuations; the solid lines indicate different values of the plasma β. An animation showing the propagation and evolution of magnetoacoustic waves is provided in the online version of this article.

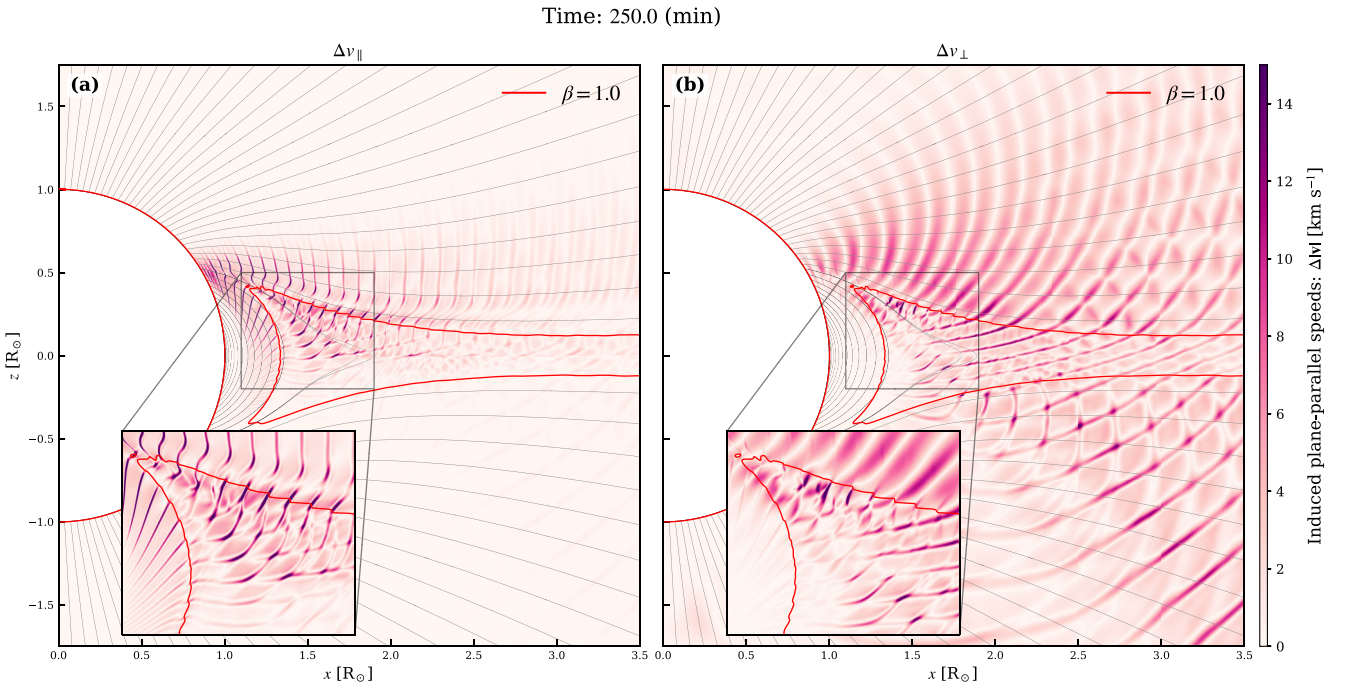

Figure 8. Decomposition of the driven plane-parallel velocities into components parallel (**left**) and perpendicular (**right**) to the local magnetic field, for the simulation with the magnetoacoustic wave driver.

Lastly, the Fourier power in the induced velocity (Δv) and resulting density fluctuations ($\Delta\rho/\rho$) is provided in Fig. 10. Here, the maximum power corresponds to a period of 5 min, which equals the driver period. The presence of higher harmonics – at 150 s, 100 s, and 75 s – is again indicative of complex wave phenomena involving successive reflections and wave interference. We further note that the locations of the peaks in density fluctuations are the same for both kinds of drivers considered in our study; however, the peaks are broader for the Alfvén driver. This broadening may be due to a number of effects

Downloaded from https://academic.oup.com/mnras/article/549/3/stag930/8679174 by Universita di Palermo - Dipartimento di Scienze Botaniche user on 06 July 2026

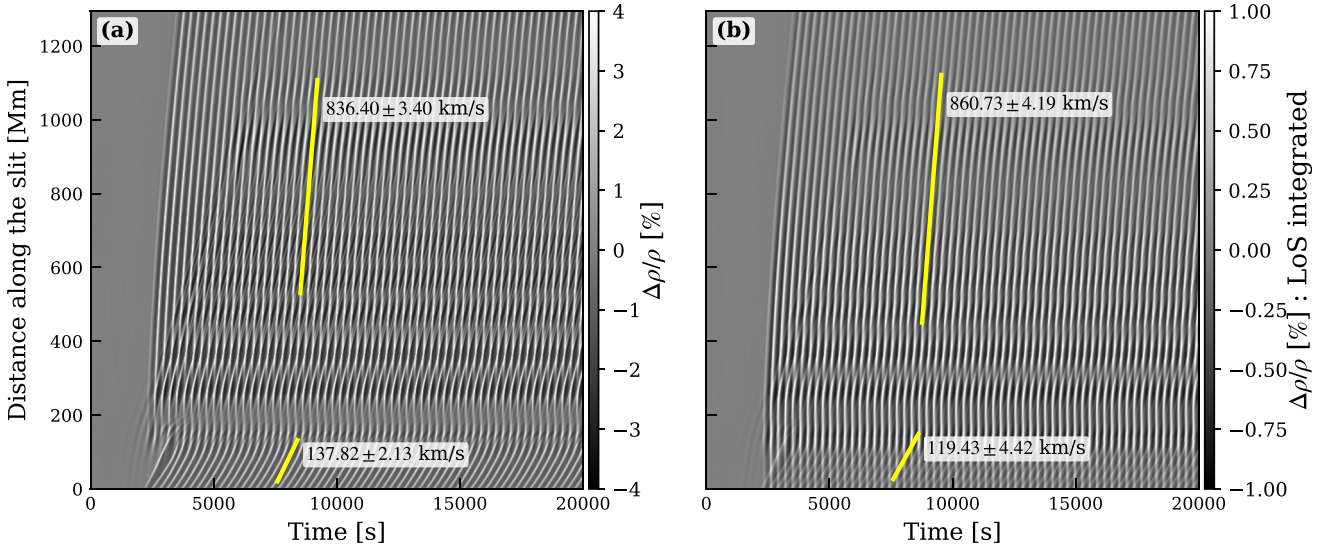

Figure 9. Time distance maps of the running difference in density (**left**) and line-of-sight integrated density (**right**) for slit 1 for the driver in the θ-direction. The yellow lines indicate the tracked bright features, used to estimate the apparent propagation speeds, also indicated alongside.

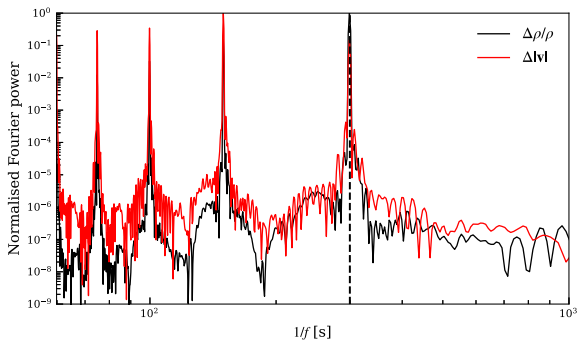

Figure 10. Normalized Fourier power for driven velocity fluctuations ($|\Delta \mathbf{v}|$; in red) and the resultant density fluctuations ($\Delta\rho/\rho$; in black). Note the presence of higher harmonics in $\Delta\rho/\rho$ is similar to Fig. 6.

that are at play in our simulations. The two simulations represent fundamentally different mechanisms of generating density fluctuations, which could have an effect on the Fourier spectra. Furthermore, the broadening may also suggest a preferential damping of the wave modes that generate the density fluctuations. A detailed discussion on the differences and similarities between the two drivers for different slits is provided in the next section.

3.3 Comparison between the drivers

As we compare Figs 2(c) (Alfvén driver) and 7(b) (magnetoacoustic driver), we note that the latter is more pronounced in the Northern Hemisphere. This can be attributed to the fact that the system responds differently to different directions of perturbation. In order to make the density fluctuations comparable in amplitude between the two cases, we halved the driver amplitude (A_0 in equation 11); note that the resulting wave amplitude is also dependent on the driving frequency, which is different in the two cases. Despite this, density fluctuations in the magnetoacoustic case have a greater amplitude (see the bright regions north of the $\beta = 0.5$ lines in Figs 2(c) and 7(b)). Due to their higher amplitudes, density fluctuations in the latter case are visible further in the domain than in the former case with an Alfvén wave driver. As expected, despite a slight mismatch in fluctuation amplitudes, their behaviour and propagation are similar as these fluctuations do not significantly alter the background.

In the previous section, we discussed the difference in the apparent propagation speed of the two wave modes along an equatorial slit. We now examine the differences in the remaining slits shown in Fig. 2(a). The time–distance maps of the running differences in line-of-sight integrated densities for these slits are shown in Fig. 11 – middle and right columns correspond to drivers along the ϕ and θ-directions, respectively, whereas the left column shows characteristic speeds along these paths; the horizontal lines mark the estimated apparent speeds for the two drivers at those locations along the slit.

As noted above, density fluctuations from both drivers are associated with magnetoacoustic waves. As slit 2 is roughly aligned with the local magnetic field (Fig. 2(a)), slow magnetoaoustic waves are expected to propagate along this slit with a propagation speed equal to the slow speed with respect to the background – $\sim 210\,\mathrm{km\,s^{-1}}$ (Fig. 11(a)). Comparing with the corresponding time–distance maps in Figs 11(b) and 11(c), there is indeed a close agreement between the estimated propagation speeds and the local speed of sound at those heights. This is also illustrated through time–distance plots depicting the arrival of slow and fast waves along this slit in Appendix C. Such a clear distinction is only possible for this slit, which completely lies in the low β region and approximately follows a magnetic field line. In this low β regime, the dominant (observable) contribution to the density fluctuations is due to slow waves, as illustrated in Appendix B. At early times in the time–distance plots, there is perhaps some evidence of the faster propagating 'daughter disturbances' (see e.g. J. Thurgood & J. McLaughlin

Downloaded from https://academic.oup.com/mnras/article/549/3/stag930/8679174 by Universita di Palermo - Dipartimento di Scienze Botaniche user on 06 July 2026

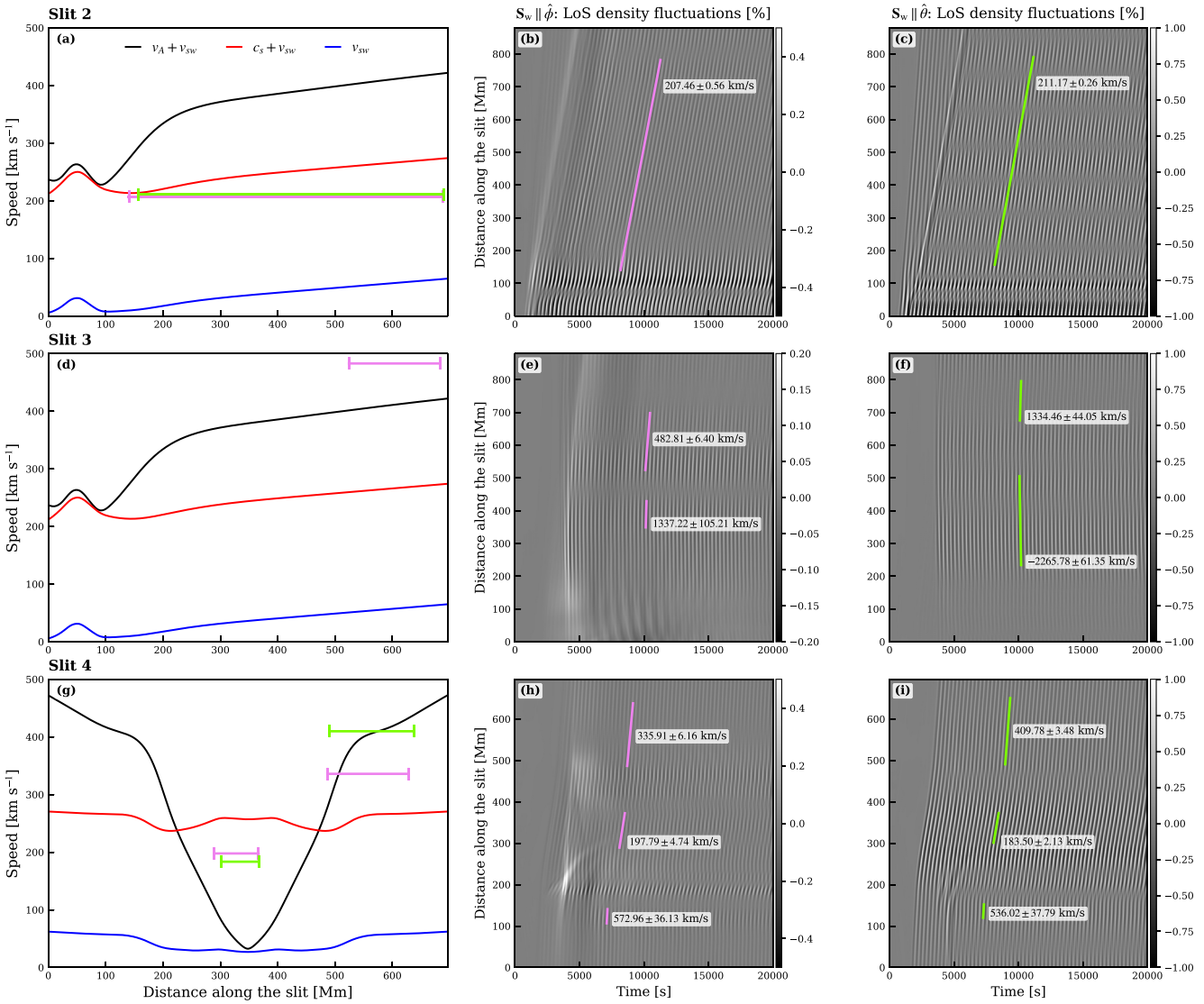

Figure 11. Time–distance maps of the line-of-sight intensity variations for different slits (in different rows); the slits are shown in Fig. 2. The middle column corresponds to the driver in the ϕ-direction (that generates Alfvén waves), whereas the right column corresponds to the driver in the θ-direction (that generates magentoacoustic waves). The adjoining left column shows characteristic speed profiles along a chosen slit.

2013), as illustrated in Appendix B, but they do not make a significant contribution to the density perturbations along this slit. We further note that Alfvén waves propagate at $\sim 450\,\mathrm{km\,s^{-1}}$ along this slit, which corresponds to the local Alfvén speed (Fig. 12).

Along slit 3, which is again placed along a magnetic field line, but in the Southern Hemisphere where waves are not excited, density fluctuations arrive almost perpendicularly from the north, after having undergone successive reflection and refraction. This results in high apparent propagation speeds along this slit (Figs 11(e) and 11(f)) which do not correlate with the speeds given in Fig. 11(d). This lack of correlation between speeds is expected as fast magnetoacoustic waves are able to propagate across magnetic field lines unlike slow magnetoacoustic and Alfvén waves.

Lastly, along a slit across the equator (slit 4), density fluctuations arrive obliquely, but the direction of approach varies in different parts of the slit. In the Northern Hemisphere where waves are driven, the density fluctuations predominantly propagate along magnetic field lines (with the slow magnetoacoustic speed) which are nearly perpendicular to this slit (see Figs 2(c) and 7(b)). As the plasma becomes gas pressure dominated close to the equator (between $\sim$ 220 and $\sim$ 480 Mm along the slit – Fig. 13), the density fluctuations propagate more obliquely, imparting a lower apparent propagation speed at mid-altitudes (Figs 11(h) and 11(i)). Finally, south of the equator, the propagation becomes more perpendicular – a consequence of driving only in the Northern Hemisphere – and we observe a small increase in the apparent propagation speed at higher altitudes.

In Fig. 14, we examine the spectral variability of the Alfvén waves (top row), the resulting density fluctuations (middle row) and the same due to a magnetoacoustic driver (bottom row) for different slits. In order to compare the relative Fourier powers for different wave modes, we have normalized each

Downloaded from https://academic.oup.com/mnras/article/549/3/stag930/8679174 by Universita di Palermo - Dipartimento di Scienze Botaniche user on 06 July 2026

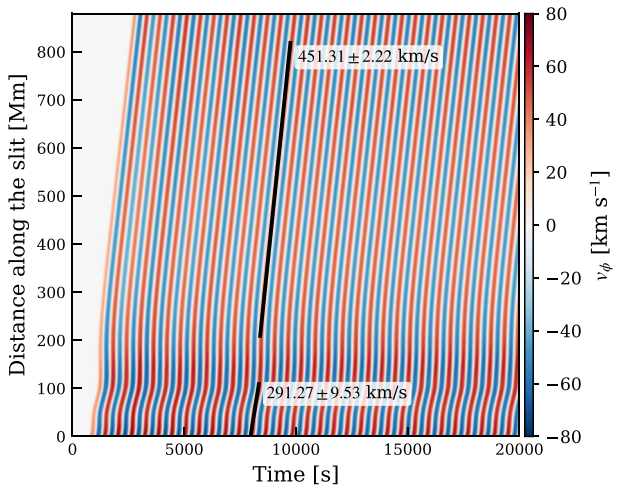

Figure 12. Time–distance map of the Alfvén wave perturbation along slit 2 (approximately parallel to the local magnetic field).

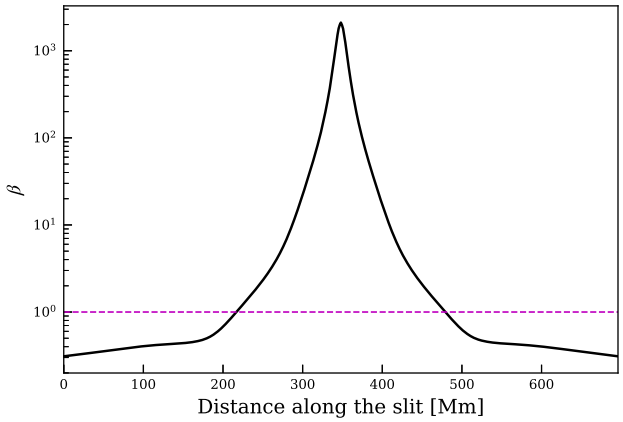

Figure 13. Plasma β profile along a slit perpendicular to the equator – slit 4.

subplot by the maximum Fourier power in its corresponding row.

Figs 14(a)–(d) depict the variation of the Fourier spectrum for Alfvén waves – peaking strongly at 10 min, equal to the driving period. For an equatorial slit, there is a loss of power beyond $\sim$ 300 Mm (Fig. 14(a)) as Alfvén waves cannot access those regions (Fig. 4(a)). Furthermore, a diffused peak may suggest continuous reflections and wave damping, as the wave power redistributes to other frequencies. Along slit 2, the waves are coherent, having a distinct peak at the driven period (Fig. 4(b)). As noted before, Alfvén waves undergo significant damping as they approach the equator, resulting in a lack of wave power visible along slit 3. Finally, the Fourier spectrum for a slit across the equator shows a mixture of the effects seen in the previous three slits – coherent waves in the Northern Hemisphere, dissipation near the equator, and finally a lack of power in the Southern Hemisphere.

The Fourier powers in Figs 10(e)–(h) for the density fluctuations peak at 5 min as a consequence of driving non-linear Alfvén waves with a 10-min periodicity. As the propagation of magnetoacoustic wave pulses is loosely independent of the local magnetic field topology, there is significant power even beyond the equator, where Alfvén waves do not reach in our simulations. Finally, we note the density fluctuations generated by applying perturbations in the latitudinal θ-direction have a similar spectrum (Figs 14(i)–(l)) to those from ϕ-direction perturbations. However, we do note that the spectra shown in the middle row have broader peaks, which may result from the associated non-linearities of the Alfvén waves.

4 DISCUSSION AND CONCLUSIONS

In this paper, we have investigated two potential mechanisms which could lead to density fluctuations in a helmet streamer, similar to the ones observed in white light by the Metis coronagraph (V. Andretta et al. 2025). Our model setup includes key global properties such as spherical expansion, gravitational stratification, thermodynamics such as thermal conduction and optically thin radiation in the presence of a supersonic and super-Alfvénic solar wind. In their study, V. Andretta et al. (2025) make a tentative link between the observed density fluctuations and p-modes based on the similarity in the frequency. In this study, we generate wave-like perturbations at the base of the corona, where we have chosen the periodicity of the generated perturbations such that the periods of the resulting density fluctuations match those observed by V. Andretta et al. (2025). Although the propagation of p-modes from the solar interior through the chromosphere is not considered, our modelling efforts shed light on how they could impact the extended corona and the solar wind, opening avenues for research concerning the energy transport mechanisms into the heliosphere.

By changing the polarization of wave-like perturbations at the base of the corona, we find that density fluctuations may be generated indirectly by non-linear Alfvén waves or directly by magnetoacoustic waves. Non-linear Alfvén waves, excited by applying perturbations in the invariant ϕ-direction, can compress the plasma indirectly via ponderomotive forces or (non-linear) phase mixing through the generation of both slow and fast waves. Perturbations in the θ-direction, on the other hand, will directly compress the plasma via the direct generation of magnetoacoustic waves. In both cases in our study, the resultant density fluctuations propagate similarly as the background remains the same. As they propagate outwards, they are affected by large radial and latitudinal variations in the background, resulting in reflection, refraction and wave confinement. For example, density fluctuations generated at the interface between open and closed field lines propagate predominantly towards regions with higher plasma β (close to the equator).

A key difference between the density fluctuations induced by the two drivers lies in how they are generated. In the case of an Alfvén wave driver, density fluctuations occur spontaneously wherever Alfvén waves exhibit non-linearity – with each point along their propagation acting as a source for magnetoacoustic pulses. It is because of this non-linear generation that the density fluctuations have a doubled frequency with respect to the Alfvén waves that excite them. On the other hand, density fluctuations are generated directly at the driver region for a magnetoacoustic wave driver and exhibit the same frequency as the driver. While the density fluctuations generated in both cases have similar behaviour in the plane of the sky, the presence of Alfvénic signatures (e.g. in Doppler velocities in the low corona or through

Downloaded from https://academic.oup.com/mnras/article/549/3/stag930/8679174 by Universita di Palermo - Dipartimento di Scienze Botaniche user on 06 July 2026

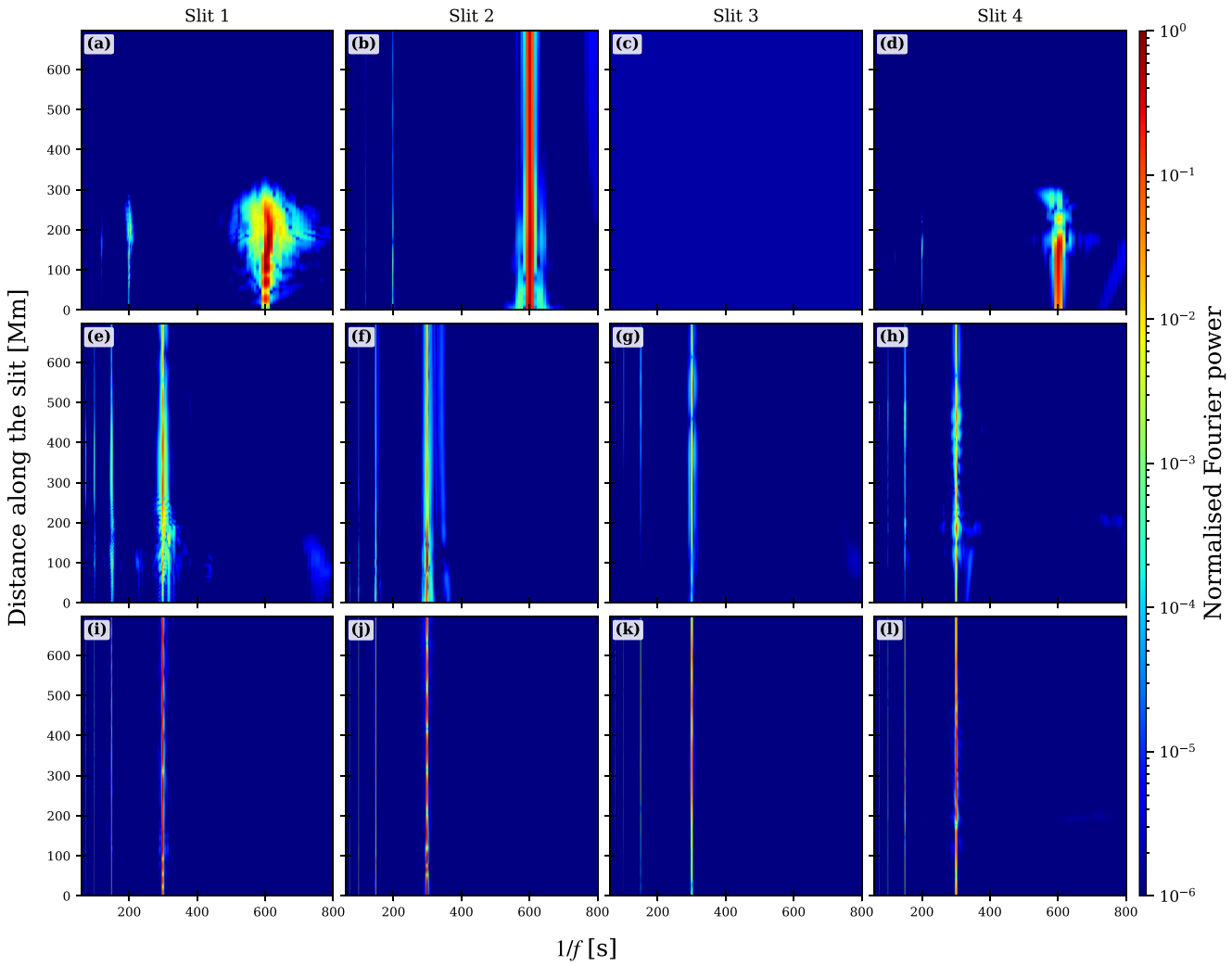

Figure 14. Fourier spectra as a function of distance along different probe slits, arranged in different columns. The top and middle rows correspond to the driver in the $\phi-$ driver, with the top row (a–d) showing Fourier powers in the driven v_ϕ component and the middle row (e–h) showing Fourier powers in the generated density fluctuations. The bottom row (i–l) corresponds to the Fourier powers in density fluctuations produced from the driver in the θ-direction. Note that powers shown in each row are normalized by the maximum power in that row.

in situ measurements in the solar wind) may be a useful diagnostic to indicate their origin.

Despite this difference in their generation mechanism, we find that the propagation of these density fluctuations is qualitatively similar in both our simulations. This results in similar time–distance maps for different slits in the domain for the two drivers and therefore a similar apparent propagation speed along chosen slits. However, as fast and slow waves travel in different directions (with respect to the magnetic field) and the (observational) slit is not necessarily aligned with the magnetic field, the time–distance maps essentially depict wave arrival at those locations in space and the calculated slopes represent the apparent propagation speeds. In our study, in order to directly compare with Metis observations, we have analysed density propagation along four different slits (shown in Fig. 2). We find that it is only for slit 2 that the apparent propagation speed roughly matches the local Alfvén and sound speed, as it is the only one somewhat aligned with the magnetic field. Other slits, on the other hand, show large variations in the apparent propagation speed – with no correlation to the Alfvén and sound speeds along the slits – but similar for both drivers.

Although still a relatively simple global model, our setup contains a range of complexities preventing the unique identification of density fluctuations as either slow or fast waves in all parts of the domain. For example, in the case of the Alfvén wave driver, in regions where there are significant cross-field variations of the Alfvén speed, density fluctuations will be generated through a combination of the non-linearity of the Alfvén waves themselves but also through phase mixing. Additionally, mode conversion from fast to slow or slow to fast waves can take place across equipartition layers (i.e. where the sound speed equals the Alfvén speed) which is also dependent on local field inclinations (H. Schunker & P. S. Cally 2006).

In general, we find that in a low-β region, the maximum contribution to the density fluctuations is from slow waves propagating along the magnetic field. These perturbations propagate at the

Downloaded from https://academic.oup.com/mnras/article/549/3/stag930/8679174 by Universita di Palermo - Dipartimento di Scienze Botaniche user on 06 July 2026

slow speed, and are clearly visible in a time–distance plot for a slit aligned with the magnetic field. In a high-β region, we found the density fluctuations to be associated with both the parallel and perpendicular velocity perturbations and hence, in these regions they are likely a mixture of both slow and fast waves. As Metis white light observations only provide information about the density and not any of the velocity components, it might not be possible to uniquely identify density fluctuations with fast or slow waves through such observations. *In situ* observations, on the other hand, might allow for separation of the parallel and perpendicular velocity perturbations and, hence, quantify their relative contributions to the density fluctuations.

The density fluctuations generated in our simulations have an amplitude – calculated via a running difference – that lies within 3−4 per cent for a cadence of 30 s. Although the fluctuation amplitudes depend on the time interval between successive outputs, their periodic nature is likely to either diminish or enhance these signals for a different output cadence. However, the (apparent) propagation speeds remain unchanged for running differences calculated at a different cadence. Furthermore, as these density fluctuations are converted to line-of-sight intensity fluctuations, we find that intensity maps typically range between 0.5 per cent and 1 per cent – similar to those reported in V. Andretta et al. (2025). Lastly, since we base the line-of-sight density integration in our study on rotational symmetry about the north–south axis (coinciding with the solar rotation axis), regions closer to the axis will have a larger contribution than regions farther away. Such an assumption holds approximately true when the Sun is surrounded by a global helmet streamer, i.e. during solar minima, when the solar magnetic field is approximately dipolar. On the other hand, during phases of higher solar activity, complex patterns of magnetic flux emergence may distort this global helmet streamer, resulting in it being confined to smaller regions.

Despite some simplifying assumptions, the simulations presented in this paper capture many of the key aspects of MHD wave propagation. Although small-scale or intermittent or transient processes such as the presence of jets, spicules, and filament eruptions will locally modify wave propagation, the global behaviour of wave propagation is likely to still contain the basic aspects of the density fluctuations described in this study. Since both Alfvén and magnetoacoustic wave modes may be generated simultaneously in the solar atmosphere (often with a broadband power spectrum), the resulting density fluctuations may be enhanced or diminished due to wave interference.

As MHD waves propagate they can transfer their energy into the solar atmosphere, contributing to coronal heating and/or solar wind acceleration. Although a detailed study of wave energy transfer is not the focus of this paper, we remark that MHD waves can also be trapped in between the generated density enhancements, thereby increasing their chances of dissipation by prolonging their activity; maximum wave trapping can occur when the density fluctuation length scale is approximately half the wavelength (A. Kumar et al. 2025). This condition is fulfilled in our simulations for density fluctuations produced from nonlinear Alfvén waves. While the density enhancements are only within 3−4 per cent and hence likely to lead to only minimal wave trapping, a continuous train of density fluctuations is likely to enhance wave trapping.

Furthermore, the highly non-uniform background of a helmet streamer provides opportunities for wave dissipation by phase mixing (J. Heyvaerts & E. R. Priest 1983). For example, in Fig. 15, we show regions in our domain where gradients in Alfvénic perturbation (v_ϕ) perpendicular to the magnetic field are greater than those parallel to the field; these are the regions where phase mixing will enhance viscous and/or resistive dissipation. We note that in our setup, such regions are more localized towards the equator and within the streamer, where non-uniformities in Alfvén wave propagation speed can generate large cross-field gradients. On the other hand, towards the poles, wave propagation speeds do not have a significant cross-field gradient, meaning that wave dissipation by phase mixing in these regions may not be as efficient as for regions closer to the equator. Apart from heating, phase mixing also generates plasma compressions in our simulations through the generation of fast waves which could also be a significant sink of Alfvén wave energy (V. Nakariakov et al. 1997; G. J. Botha et al. 2000; J. Thurgood & J. McLaughlin 2013).

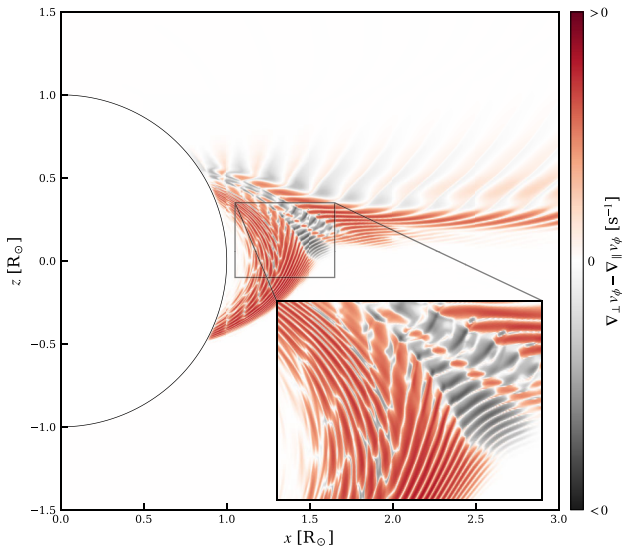

Figure 15. Difference between gradients of the Alfvén wave component (v_ϕ) across ($\nabla_\perp v_\phi$) and parallel ($\nabla_\parallel v_\phi$) to the local magnetic field. The red regions, where $\nabla_\perp v_\phi - \nabla_\parallel v_\phi > 0$, are the regions where wave dissipation by phase mixing is likely to be most significant.

ACKNOWLEDGEMENTS

AK and SD-Y received funding from the Leverhulme Trust (RPG-2021-114). TAH received funding from the Carnegie Trust grant number RIG013386. PP acknowledges support by the Italian PRIN 2022, project 2022294WNB entitled 'Heliospheric shocks and space weather: from multispacecraft observations to numerical modeling', funded by Next Generation EU, within Piano Nazionale di Ripresa e Resilienza (PNRR), Missione 4 'Istruzione e Ricerca' – Componente C2 Investimento 1.1, 'Fondo per il Programma Nazionale di Ricerca e Progetti di Rilevante Interesse Nazionale (PRIN)'. VA acknowledges support by Addendum n. 1 to the ASI-INAF agreement n. 2018-30-HH.0 for the science support to Metis, SWA DPU e STIX in the D/E phases. The authors also thank the referee for their valuable comments.

DATA AVAILABILITY

The data presented in this article will be available from the University of St Andrews research repository.

Downloaded from https://academic.oup.com/mnras/article/549/3/stag930/8679174 by Universita di Palermo - Dipartimento di Scienze Botaniche user on 06 July 2026

REFERENCES

Andretta V. et al., 2025, A&A, 701, A199
Banerjee D., Pérez-Suárez D., Doyle J., 2009, A&A, 501, L15
Banerjee D. et al., 2021, Space Sci. Rev., 217, 1
Botha G. J., Arber T., Nakariakov V., Keenan F., 2000, A&A, 363, 1186
Callingham H., De Moortel I., Pagano P., 2024, MNRAS, 535, 1640
Cirtain J. et al., 2007, Science, 318, 1580
De Pontieu B. et al., 2007, Science, 318, 1574
Felipe T., Sangeetha C., 2020, A&A, 640, A4
Heyvaerts J., Priest E. R., 1983, A&A, 117, 220
Hollweg J. V., Jackson S., Galloway D., 1982, Sol. Phys., 75, 35
Horbury T. S. et al., 2020, ApJS, 246, 45
Huang Z. et al., 2026, ApJ, 999, L4
Jefferies S. M., McIntosh S. W., Armstrong J. D., Bogdan T. J., Cacciani A., Fleck B., 2006, ApJ, 648, L151
Jess D., Morton R., Verth G., Fedun V., Grant S., Giagkiozis I., 2015, Space Sci. Rev., 190, 103
Jess D. B., Jafarzadeh S., Keys P. H., Stangalini M., Verth G., Grant S. D., 2023, Living Rev. Sol. Phys., 20, 1
Klimchuk J., Patsourakos S., Cargill P., 2008, ApJ, 682, 1351
Kumar A., Howson T. A., Pagano P., De Moortel I., 2025, MNRAS, 541, 2843
Lionello R., Linker J. A., Mikić Z., 2008, ApJ, 690, 902
McIntosh S. W., De Pontieu B., 2012, ApJ, 761, 138
Mignone A., Bodo G., Massaglia S., Matsakos T., Tesileanu O. e., Zanni C., Ferrari A., 2007, ApJS, 170, 228
Mikić Z., Lionello R., Mok Y., Linker J. A., Winebarger A. R., 2013, ApJ, 773, 94
Morton R., Tomczyk S., Pinto R., 2016, ApJ, 828, 89
Morton R., Weberg M., McLaughlin J., 2019, Nat. Astron., 3, 223
Morton R., Gao Y., Tajfirouze E., Tian H., Van Doorsselaere T., Schad T., 2026, Nat. Astron., 10, 42
Morton R. J., Soler R., 2025, ApJ, 986, L6
Nakariakov V., Roberts B., Murawski K., 1997, Sol. Phys., 175, 93
Parenti S., Réville V., Brun A. S., Pinto R. F., Auchère F., Buchlin E., Perri B., Strugarek A., 2022, ApJ, 929, 75
Parker E. N., 1958, ApJ, 128, 664
Pascoe D. J., De Moortel I., Pagano P., Howson T. A., 2022, MNRAS, 516, 2181
Priest E., 2014, Magnetohydrodynamics of the Sun. Cambridge Univ. Press, Cambridge UK
Réville V., Tenerani A., Velli M., 2018, ApJ, 866, 38
Schunker H., Cally P. S., 2006, MNRAS, 372, 551
Spruit H., Bogdan T., 1992, ApJ, 391, L109
Stangalini M., Del Moro D., Berrilli F., Jefferies S., 2011, A&A, 534, A65
Thurgood J., McLaughlin J., 2013, Sol. Phys., 288, 205
Van Ballegooijen A., Asgari-Targhi M., Cranmer S., DeLuca E., 2011, ApJ, 736, 3
Van Damme H., De Moortel I., Pagano P., Johnston C. D., 2020, A&A, 635, A174
Verwichte E., Nakariakov V., Longbottom A., 1999, J. Plasma Phys., 62, 219
Weberg M. J., Morton R. J., McLaughlin J. A., 2018, ApJ, 852, 57
Yuan D., Pascoe D. J., Nakariakov V. M., Li B., Keppens R., 2015, ApJ, 799, 221

SUPPORTING INFORMATION

Supplementary data are available at *MNRAS* online.

Streamer_Evolution.mp4
MA_Waves.mp4
Beta_10.mp4
Beta_1.mp4
Beta_001.mp4
Alfven_Waves.mp4

Please note: Oxford University Press is not responsible for the content or functionality of any supporting materials supplied by the authors. Any queries (other than missing material) should be directed to the corresponding author for the article.

APPENDIX A: DENSITY FLUCTUATIONS FOR DIFFERING PLASMA β REGIMES

Following the approach of E. Verwichte et al. (1999), we use simple 2D simulations to demonstrate the effect of the plasma β on the density fluctuations associated with Alfvén waves in a non-linear regime due to ponderomotive effects ($\mathbf{F}_p \sim -\nabla B_\perp^2$, $B_\perp$ being the perturbed magnetic field component in the invariant direction).

Here, we have considered a uniform medium with a magnetic field aligned with the y-axis; the Alfvén speed is set to unity and the pressure is adjusted according to a given value of the plasma β. An initial non-linear Alfvén perturbation in velocity (v_z, corresponding to the invariant direction out of the simulation plane) is applied at the centre of the domain. Fig. A1 depicts the evolution of density fluctuations in the domain (from left to right), whereas Fig. A2 compares their amplitudes at an intermediate time. In Fig. A1, the left column shows the initial state with only the applied Alfvén pulse (white contour) and the background magnetic field (blue streamlines) whereas the other two columns show the induced velocities in the plane (yellow arrows) and the associated density fluctuations.

Slow and fast mode waves are generated due to ponderomotive effects, which propagate at their respective characteristic phase speeds. In the low β regime (top row), the largest contribution to the density fluctuations comes from slow waves that follow the magnetic field lines, lagging behind the Alfvén pulse. An initial Alfvén pulse with a weakly non-linear amplitude of $0.1v_A$ is chosen in all cases. Comparing the results for different values of β, we can clearly see that the amplitude of the resultant density fluctuations is higher when the medium has a lower plasma β.

Downloaded from https://academic.oup.com/mnras/article/549/3/stag930/8679174 by Universita di Palermo - Dipartimento di Scienze Botaniche user on 06 July 2026

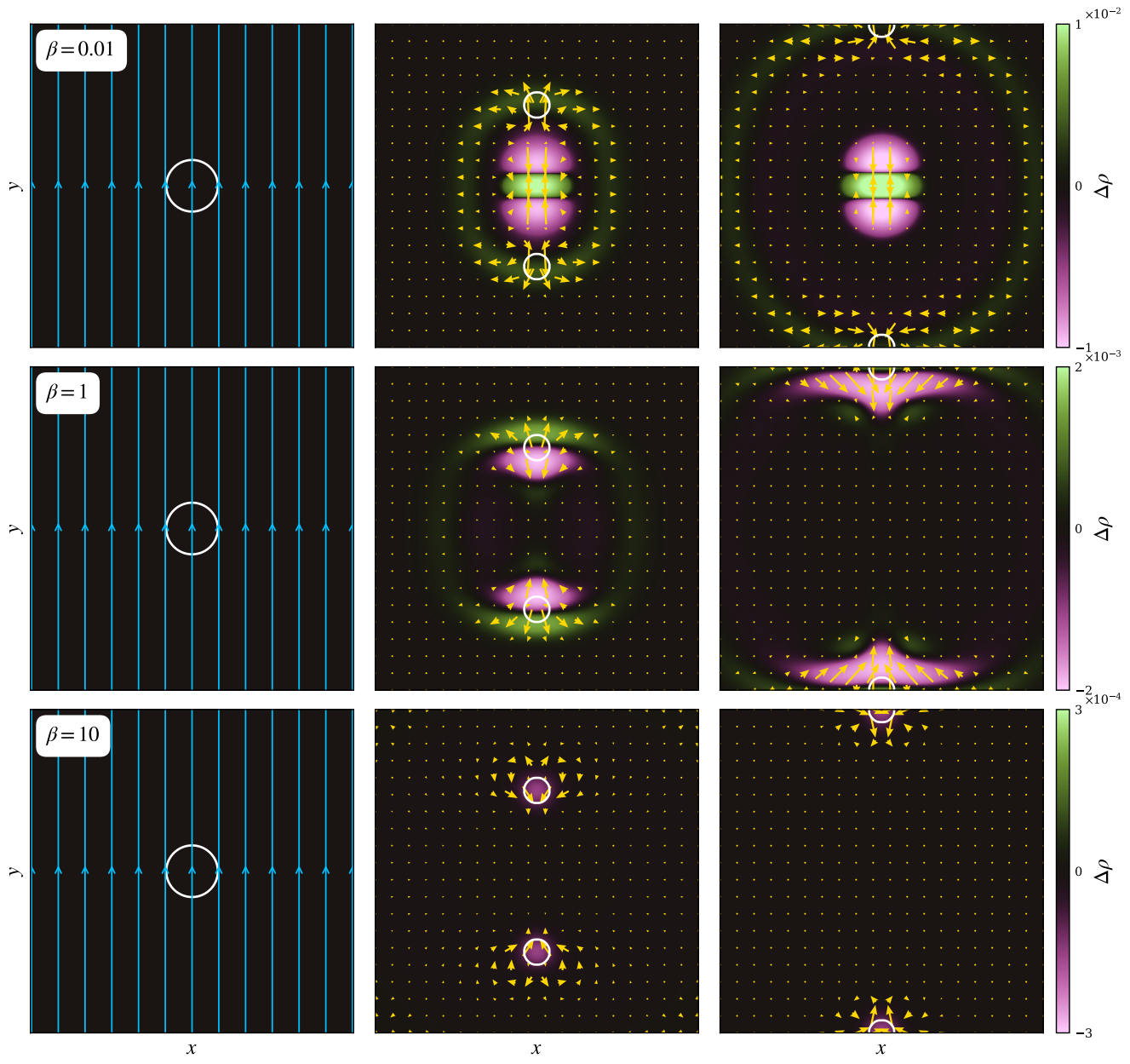

Figure A1. Evolution of induced density fluctuations for a weakly non-linear Alfvénic pulse (from left to right) for different values of the background plasma β (top to bottom). The medium is uniform and has magnetic field aligned with the y-axis (shown by the blue streamlines in the left column). The white contours indicate the location of the Alfvén pulse. The yellow arrows denote the induced plane-parallel velocities due to the imposed pulse. Animations corresponding to these figures are provided in the online version of the article.

Downloaded from https://academic.oup.com/mnras/article/549/3/stag930/8679174 by Universita di Palermo - Dipartimento di Scienze Botaniche user on 06 July 2026

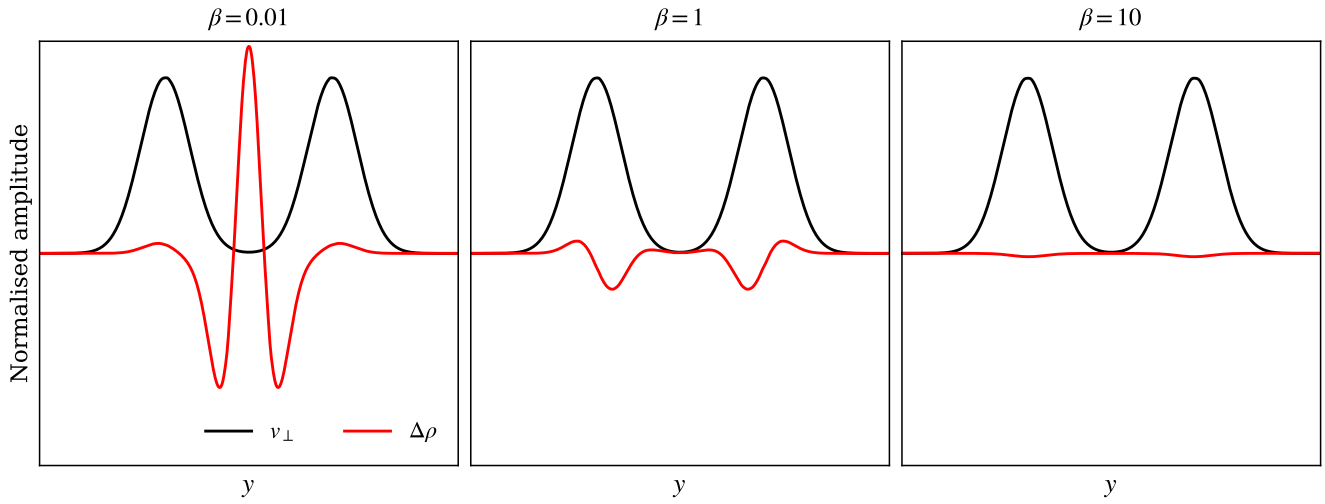

Figure A2. Comparison between density fluctuations generated due to the same non-linear Alfvénic pulse in media with differing values of the plasma β. The Alfvénic pulse (black) and density fluctuations (red) are plotted along a magnetic field line and are normalized for visualization purposes. Larger density fluctuations are produced for lower values of β.

APPENDIX B: DENSITY FLUCTUATIONS INDUCED BY A SHORT ALFVÉN WAVE TRAIN

A non-linear Alfvén wave continuously generates fast and slow mode waves along its path of propagation through the ponderomotive force and non-linear phase mixing. Here we use the same setup as in the main body of the paper but restrict the driven Alfvén wave to just five wave periods to simplify the interpretation of the associated density fluctuations. Fig. B1(a) shows the density fluctuations (white and black contours) and the Alfvén wave (blue and red contours). Figs B1(b) and (c) show the corresponding decomposed parallel and perpendicular velocity components. In a low-β regime, these correspond to the slow and fast waves, respectively. In the low β regime just north of the helmet streamer, the parallel velocity component shows perturbations which propagate with the Alfvén waves (referred to as 'daughter disturbances' by e.g. J. Thurgood & J. McLaughlin 2013) as well as perturbations which lag behind. These latter perturbations correspond to a slow wave as in a low-β region the sound speed is lower than the Alfvén speed. Comparing the perturbations in the parallel velocity in this region with the density perturbations in the LHS panel, it is clear that the slow wave is the dominant contributor to the density fluctuations. Therefore, when probing along a magnetic field line in a low β regime (see e.g. Fig. 11(b)), the strongest density fluctuations appear to be associated with slow waves. In low β regions, the density fluctuations associated with the perpendicular velocity component (fast waves) are generally weaker than those associated with the parallel velocity perturbations (slow waves). In contrast, in the region above the helmet streamer, which is a high β region, the strongest density perturbations are associated with the perpendicular velocity perturbations.

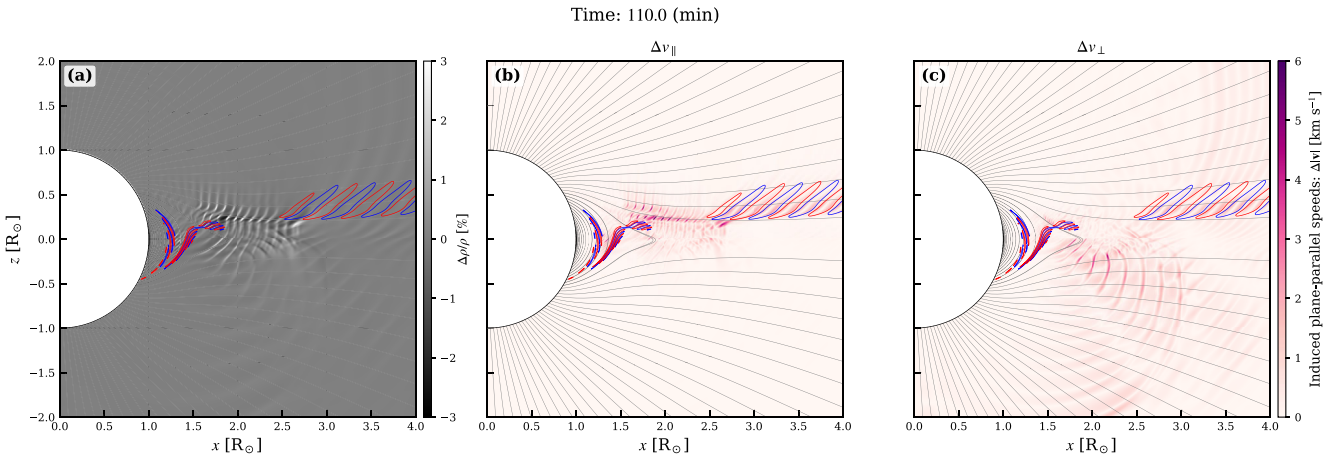

Figure B1. A snapshot showing the propagation of **(a)** density fluctuations, **(b)** the parallel and **(c)** perpendicular components of the velocities in the plane of the simulation. The red and blue contours show the Alfvén wave train (that is only five wavelengths long) considered for this simulation.

Downloaded from https://academic.oup.com/mnras/article/549/3/stag930/8679174 by Universita di Palermo - Dipartimento di Scienze Botaniche user on 06 July 2026

APPENDIX C: ADDITIONAL TIME–DISTANCE PLOTS FOR SLITS 1 AND 2

In this appendix, we look in more detail at the time–distance plots along slits 1 and 2 for the Alfvén wave driver (see Fig. 2(a)). Through non-linear effects, the Alfvén waves produce both fast and slow waves which lead to density fluctuations throughout the domain. However, different regions in the domain have different amounts of slow and fast mode contribution.

Fig. C1 shows the density perturbations (panel (a)) and parallel (panel (b)) and perpendicular (panel (c)) velocity components. The lower part of this slit (below approximately 300 Mm) goes through a $\beta < 1$ region whereas the rest of the slit is in a high-beta regime. In the lower part, it is clear that the density fluctuations correspond to the slow wave (the parallel velocity component). In the middle, both the parallel and perpendicular components are roughly equal in amplitude, and hence the density perturbations will be a mixture of slow and fast waves. In the upper regions of the slit, the dominant velocity component is the perpendicular one implying the density fluctuations are mostly associated with the fast wave.

Fig. C2 shows the same variables along slit 2. This slit mostly goes through a low-beta region and, particularly for its upper half, more or less aligns with the magnetic field. In this region, it is clear that the dominant velocity component is the parallel one and hence, given the low plasma β, that the density perturbations are mostly due to the slow wave. This is also confirmed by the similarity between the apparent propagation speed of the parallel velocity component and the density fluctuations along this slit.

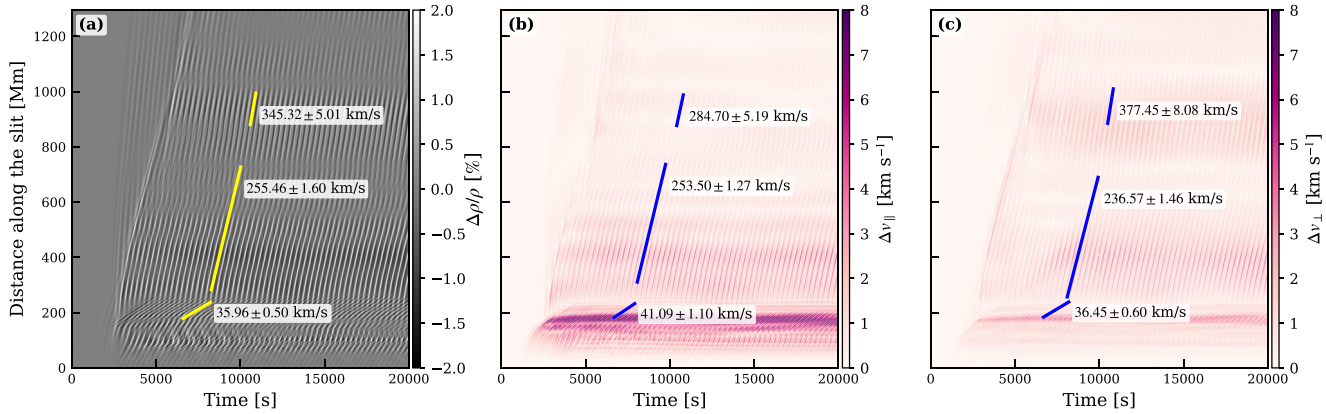

Figure C1. Time–distance plots of the density fluctuations (panel (a)) and the parallel (panel (b)) and perpendicular (panel (c)) velocity components for slit 1 of the Alfvén wave driver (see Fig. 2(a)).

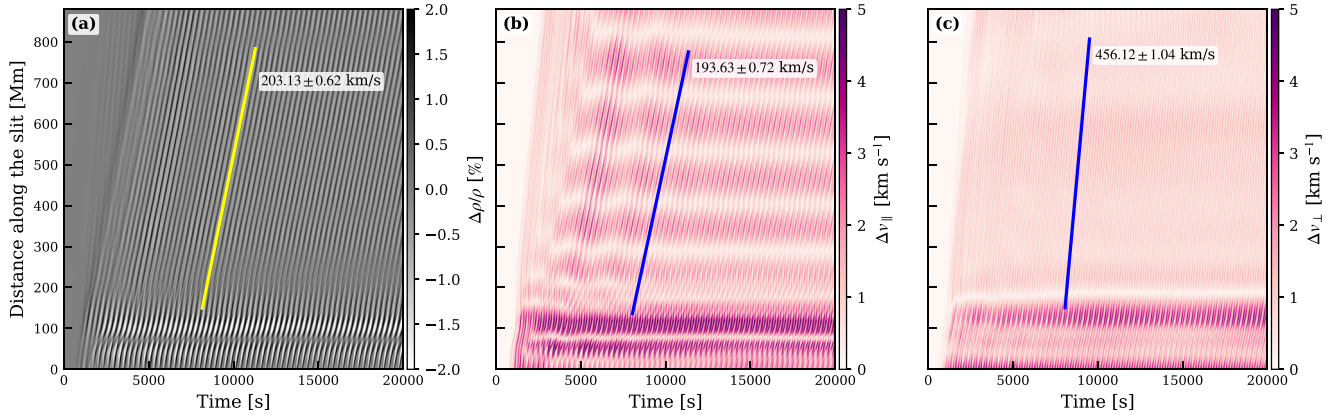

Figure C2. Time–distance plots of the density fluctuations (panel (a)) and the parallel (panel (b)) and perpendicular (panel (c)) velocity components for slit 2 of the Alfvén wave driver (see Fig. 2(a)).

This paper has been typeset from a TEX/LATEX file prepared by the author.

© The Author(s) 2026.
Published by Oxford University Press on behalf of Royal Astronomical Society. This is an Open Access article distributed under the terms of the Creative Commons Attribution License (https://creativecommons.org/licenses/by/4.0/), which permits unrestricted reuse, distribution, and reproduction in any medium, provided the original work is properly cited.

Downloaded from https://academic.oup.com/mnras/article/549/3/stag930/8679174 by Universita di Palermo - Dipartimento di Scienze Botaniche user on 06 July 2026